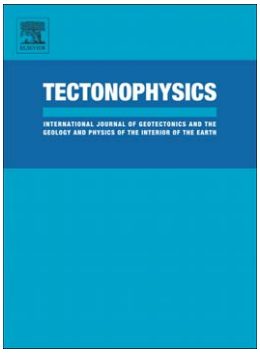

The effects of pre-existing discontinuities on the surface expression of normal faults: Insights from wet-clay analogue modeling

Lorenzo Bonini, Roberto Basili, Giovanni Toscani, Pierfrancesco Burrato, Silvio Seno, Gianluca Valensise

PII: S0040-1951(15)00678-2
DOI: doi: 10.1016/j.tecto.2015.12.015
Reference: TECTO 126880

To appear in: *Tectonophysics*

Received date: 1 June 2015
Revised date: 22 October 2015
Accepted date: 12 December 2015

Please cite this article as: Bonini, Lorenzo, Basili, Roberto, Toscani, Giovanni, Burrato, Pierfrancesco, Seno, Silvio, Valensise, Gianluca, The effects of pre-existing discontinuities on the surface expression of normal faults: Insights from wet-clay analogue modeling, *Tectonophysics* (2016), doi: 10.1016/j.tecto.2015.12.015

The effects of pre-existing discontinuities on the surface expression of normal faults: insights from wet-clay analogue modeling

Lorenzo Bonini[1]*, Roberto Basili[2], Giovanni Toscani[3], Pierfrancesco Burrato[2], Silvio Seno[3], Gianluca Valensise[2]

1 Dipartimento di Matematica e Geoscienze, Università di Trieste, ITALY

2 Istituto Nazionale di Geofisica e Vulcanologia, Rome, ITALY

3 Dipartimento di Scienze della Terra e dell'Ambiente, Università di Pavia, Pavia, ITALY

Corresponding author: *Lorenzo Bonini, e-mail address: lbonini@units.it*

ABSTRACT

We use wet-clay analogue models to investigate how pre-existing discontinuities (i.e. structures inherited from previous tectonic phases) affect the evolution of a normal fault at the Earth's surface. To this end we first perform a series of three reference experiments driven by a 45° dipping master fault unaffected by pre-existing discontinuities to generate a mechanically isotropic learning set of models. We then replicate the experiment six times introducing a 60°-dipping precut in the clay cake, each time with a different attitude and orientation with respect to an initially-blind, 45°-dipping, master normal fault. In all experiments the precut intersects the vertical projection of the master fault halfway between the center and the right-hand lateral tip. All other conditions are identical for all seven models. By comparing the results obtained from the mechanically

isotropic experiments with results from experiments with precuts we find that the surface evolution of the normal fault varies depending on the precut orientation. In most cases the parameters of newly-forming faults are strongly influenced. The largest influence is exerted by synthetic and antithetic discontinuities trending respectively at 30° and 45° from the strike of the master fault, whereas a synthetic discontinuity at 60° and an antithetic discontinuity at 30° show moderate influence. Little influence is exerted by a synthetic discontinuity at 45° and an antithetic discontinuity at 60° from the strike of the master fault. We provide a ranking chart to assess fault-to-discontinuity interactions with respect to essential surface fault descriptors, such as segmentation, vertical-displacement profile, maximum displacement, and length, often used as proxies to infer fault properties at depth. Considering a single descriptor, the amount of deviation induced by different precuts varies from case to case in a rather unpredictable fashion. Multiple observables should be taken into consideration when analyzing normal faults evolving next to pre-existing discontinuities.

1. INTRODUCTION

Understanding how a normal fault evolves over time and how its geometry can be reconstructed from its surface evidence has been discussed at length in the literature. The most common way to describe a surface fault and to discuss its evolution is through three parameters: the maximum displacement (Dmax), the total length of the surface trace (L), and the displacement distribution along the fault trace. Relationships between these parameters and their variations over time and space have been extensively investigated (e.g., Schlische et al., 1996; Kim and Sanderson, 2005, and references therein; Torabi and Berg, 2011) and are often used to derive parameters that are unknown or cannot be directly measured. For instance, in active tectonics studies, Dmax, L, or displacement distribution profiles are often used to speculate about segmentation processes and then estimate the magnitude of either future or past earthquakes using empirical relationships (e.g., Wells and Coppersmith, 1994; Wesnousky, 2008; Leonard, 2014). It is well known, however, that 1) the degree of development of faults at the surface combined with 2) local geological conditions may complicate our understanding on the real geometry or behavior of faults at depth using empirical relationships or theoretical models (e.g. Cowie and Shipton, 1998; Bonini et al., 2014; Leonard, 2014). Concerning the first point, we know that faults evolve through different development stages. At immature stages a fault may be confined at depth; its surface evidence may consist of folds and secondary fractures associated with bending of the topographic surface (e.g. bending moment faults). At mature stages a fault is usually well expressed at the surface, its plane usually bounding a sedimentary basin (Gawthorpe and Leeder, 2000). As for the second point, the mechanical characteristics, the spatial distribution of different rock types and presence of pre-existing discontinuities (either faults or fractures) are first-order factors that alter the isotropy of host rocks which may subsequently affect fault development (e.g. Nicol et al., 1996; Tavarnelli et al., 2003).

The superposition of extensional fault systems derived by diachronic, non-coaxial, deformation phases is commonly observed in nature. This may happen in either of two cases: 1) regions that underwent multiple

extensional phases, e.g. the North Sea (e.g., Whipp et al., 2014), Thailand (e.g., Morley et al., 2004), the East African rift system (e.g., Lezzar et al., 2002; Bonini et al., 2007; Corti et al., 2007), South Africa (Paton, 2006); or 2) regions where extensional phases are separated by a contractional phase (orogenic cycle), e.g. the Apennine (e.g., Hyppolite et al., 1994; Tavarnelli et al., 2001; Tavarnelli and Prosser, 2003), the Alps (e.g., Selverstone, 1988; Bonini et al., 2010; Decarlis et al., 2013), the Basin and Range in the western United States (e.g., Wernicke, 1981; Malavieille, 1993), the Taiwan Orogen (e.g., Teng, 1996).

In this study we use analogue models to investigate how pre-existing discontinuities, potentially formed under a different stress field or paleogeographic configuration, affect the surface expression of new normal faults. To this end we first carry out a series of mechanically isotropic experiments, aimed at building up an observation set for learning how an initially-blind normal fault develops before daylighting and beyond. Then, we repeat the experiments by introducing variously-oriented discontinuities and analyze their effect on the development of the surface fault properties.

2. METHOD

2.1. Modeling approach

Few materials are considered suitable to simulate extension in scaled physical models. Among them, dry granular materials (e.g. quartz sand) and wet clay are the most commonly used. How rheological differences between these two classes of materials affect modeling observations is a long-debated issue. Several investigators compared results obtained using wet and dry materials, concluding that both can be used (e.g., Eisenstadt and Sims, 2005; Withjack and Schilsche, 2006; Withjack et al., 2007; Bonini et al., 2014) taking into account their specificities, e.g. dry sand does not behave as an ideal frictional-plastic material and clay has high cohesion preventing gravitational collapses (Mandl, 2000). Eisenstadt and Sims (2005) analyzed such differences also for tectonic inversion models, indicating that both wet and dry materials are good analogues, but wet clay is more appropriate than dry granular materials for simulating tectonic inversion/fault

reactivation. As of today, however, dry granular materials are the most used experimental methods to study the role of pre-existing faults (see Bonini et al., 2012 for a review). In these studies thin mechanical discontinuities are simulated by introducing thin weak layers of materials with less friction or strength than the dry granular materials representing fault-hosting rocks (e.g., Sassi et al., 1993; Bonini et al., 2011: Ahmad et al., 2014; Toscani et al., 2014; Di Domenica et al., 2014; Faccenna et al., 1995; Bonini, 1998; McClay et al., 2000; Dubois et al., 2002; Gartrell et al., 2005; Del Ventisette et al., 2005, 2006; Konstantinovskaya et al., 2007; Sani et al., 2007; Cerca et al., 2010; Pinto et al., 2010). Alternatively, another technique consists in extending the model before compressing it, in case of positive inversion, or the opposite, in case of negative inversion (e.g., McClay, 1989; Withjack et al., 2007; Marques and Nogueira, 2008). So far, wet-clay models have not been much used because the only known method for introducing pre-existing discontinuities was to pre-form the material before the experiment (e.g., Henza et al., 2010). This limitation has been recently overcome with a novel method enabling the modeler to introduce thin weaknesses in wet clay by precutting the material with an electrified blade (Cooke et al., 2013; Bonini et al., 2014; Bonini et al., 2015; Hatem et al., 2015). The low voltage current running through the blade helps to break the van der Waals bonds within the clay mixture and limits the dragging, thereby preserving the initially imposed shape. Moreover, these precuts are especially suitable to simulate pre-existing faults because the friction onto their interface is the same as that of faults that form in wet clay. This novel technique allows the modeler to introduce very thin discontinuities in an easier and more accurate way than in other modeling setups based on granular materials, and to effectively simulate natural fault zones represented by a small gap between the fault blocks. Considering the specific goal of our study, that involves the simulation of pre-existing high-angle discontinuities with various orientations with respect to an initially blind, extensional fault, we adopt the wet clay as the analogue material and use an electrified cutter to introduce pre-existing discontinuities.

2.2. Experimental apparatus and scaling

The experimental apparatus consists of a clay box with an inclined plane representing the master fault plane (Fig. 1). Motion on the fault is restricted to the central and inclined part of the box and guided by a mobile rigid sheet pulled by a stepper motor. The fault footwall is made up by a rigid block. Above this block lies the analogue material, i.e. the wet clay. As a clay type we use kaolin, the preferred clay for analogue modeling (e.g. Eisenstadt and Sims, 2005; Henza et al., 2010; Cooke and van der Elst, 2012), and specifically the CC31 China Clay (see data in the Appendix). The master fault dip is set at 45° based on worldwide compilations of normal faults showing that this is the most common value in tectonically active regions (Jackson and White, 1989; Collettini and Sibson, 2001).

For a proper scaling of our experiments we use geometric, kinematic, and dynamic similarity relationships (Hubbert, 1937; Ramberg, 1981). Our mixture of wet kaolin has a 60% of water content by mass; as a result it has a density of 1.65 g/cm^3. With this water content, we may assume a cohesion in a range of 60-140 Pa (Eisenstadt and Sims 2005). Consequently, the scaling relationship can be calculated as

$$C^* = \rho^* L^* \quad (1)$$

where C^*, ρ^*, and L^* are the model-to-prototype ratios for cohesion, density, and length, respectively. As a natural analogue we assume a rock with a density of 2500 kg/m^3 and a cohesion 10-20 MPa, so that the length ratio varies from 10^{-4} to 10^{-5}. Hence, assuming eq. (1) 1 cm in our model corresponds to about 0.1-1.0 km in nature. Particular care is also devoted to properly select the velocity at which the rigid sheet – i.e. the analogue of the master fault - is moved during the experiments. We chose a strain rate of 0.3 mm/min (0.005 mm/s) because it is in the range allowing wet kaolin to deform as a biviscoelastic Burgers material, i.e. the long-term behavior of the natural rocks (Cooke and van der Elst, 2012). At this strain rate the frictional coefficient of wet kaolin is about 0.6 (Henza et al., 2010) that is similar to the frictional coefficient of rocks at slow slip rate, 0.55 and 0.85 (e.g., Handin, 1966; Byerlee, 1978). Since the procedure used to carry out the precut neither alters the

chemical properties of the kaolin mixture, nor changes its water content, we assume that the frictional coefficient along the precut is the same as that of faults that naturally form in wet kaolin.

As the kaolin is a platy mineral, we ensure isotropic behavior by kneading the wet clay before laying it down into the experimental apparatus. Mechanical properties of wet kaolin are sensitive to the water content (Cooke and van der Elst, 2012), hence we devote special care to keep it constant throughout the experiment. We thus measured the water content before and after running all experiments and verified that the water loss was always negligible (< 1%). Thence we assume that the same mechanical behavior persists throughout the experiments.

2.3. Modeling strategy

The first goal of the modeling is to validate our method in simulating a natural normal fault in mechanically isotropic conditions, to verify the reproducibility of the method, and to estimate the aleatory variability of the results. We thus perform three experiments (E1A, E1B, and E1C) with an identical setup. For all experiments, we identify three stages of development at the end of regular intervals of 0.5 cm of displacement along the master fault plane. Each interval is denoted as: Early Stage, up to 0.5 cm; Middle Stage, up to 1.0 cm; and Late Stage, up to 1.5 cm (Fig. 2). We stop the experiments after 1.5 cm of total displacement on the master fault because the traces of main newly-formed surface faults reach close to the border of the region that we consider suitable to avoid boundary effects (Figs. 2 and 3), hereinafter named “Region Of Interest” (ROI; Fig. 1).

The second and main goal of the modeling is to evaluate the effects of precuts in the development of new surface faults and analyze similarities and differences with respect to the results obtained in the isotropic experiment. We thus carry out six different experiments in which a precut - the laboratory analogue of a natural discontinuity - is introduced halfway between the center and the right-hand lateral tip of the master fault. The models have been built in such a way as to perform, as far as possible, the intersection between the precut and the master fault in the same position. The precut takes a different orientation with respect to the

master fault in each experiment (Fig. 4). In the first three experiments (E2, E3 and E4) the precut forms an angle of 30°, 45° and 60° with respect to the strike of the master fault and has a synthetic attitude. In the other three experiments (E5, E6 and E7) the precut has the same strike as in the previous experiments but its attitude is antithetic with respect to the master fault. All the precuts extend down to the rigid footwall, and dip at 60°, i.e. steeper than the master fault because they simulate pre-existing faults formed in the uppermost level of the brittle crust where a steeper dip of new normal faults can be expected.

To monitor and analyze all experiments, we take photographs and structured-light scans of the free surface of the models at regular intervals, respectively every 0.1 cm and 0.5 cm of displacement on the master fault. The scans provide a record of the hanging wall subsidence and of the displacement of major faults extracted from 18 profiles perpendicular to the strike of the master fault (Fig. 1). The photographs allow us to calculate the displacement field and the strain distribution at the free surface of the model using the PIVLab software, based on the Digital Image Correlation (D.I.C.) method (Garcia, 2011; Thielicke, 2014; Thielicke and Stamhuis, 2014). D.I.C. is based on the optical comparison between image pairs, hence its accuracy depends on the resolution of the photographs and on the color contrast. For our photographs we choose a resolution of 18 megapixel, an acceptable compromise between file size and optical quality. To increase the color contrast we sprinkle black quartz sand on the model free surface before starting the experiments. The size of the interrogation area for the D.I.C. calculations is 50x50 pixel (1 pixel is 0.075 mm).

3. EXPERIMENTAL RESULTS

3.1. Isotropic experiments (E1A, E1B, E1C)

This section presents the results of three isotropic experiments: E1A, E1B, and E1C. For simplicity and to avoid repetitions, the following detailed description uses the first experiment, E1A (Fig. 2) only. The rest of the analysis considers the results of all three experiments together.

In the Early Stage, small fractures form at the free surface of the clay model spreading over the entire length of the master fault and beyond. Topography and slope analyses indicate that these structures have not developed a detectable vertical offset and appear to be related to the bending moment generated by the surface warping due to the displacement of the master fault at depth (Figs. 2a, and 2b). We consider these brittle structures as representative of the embryonic phase of bending-moment faults. The D.I.C. analysis shows that the displacement vectors are parallel to the slip imposed on the master fault in the central part of the ROI and tend to rotate progressively inward near the master fault tips and toward the ROI boundary (Fig. 2c). This pattern is evident also from the strike-parallel component of displacement, which increases sideways from the fault center point (Fig. 2d). The strain analysis shows that most of the deformation concentrates in the area affected by the bending moment and by the fractures (Fig. 2e).

In the Middle Stage few synthetic faults form with a length similar to that of the small fractures formed during the previous stage (Fig. 2f). These faults are perpendicular to the direction of maximum extension in the central part of the ROI and rotate inward at their lateral tips. From the shape of the free surface, the displacement field analysis and the strain distribution it is evident that most of the activity of these faults occurs within the sector corresponding to the surface projection of the buried master fault. The curvature of the fault trace corresponds to the region where the surface displacement is not parallel to the main slip direction on the master fault (Figs. 2h, 2i). The D.I.C. analysis also shows that no horizontal displacement is detected in the footwall of the surface faults, indicating full decoupling between the two parts of the model separated by the fault zone. The vertical displacement along the surface faults indicates two peaks located near the right- and left-hand tips of the master fault (Fig. 2i). The strain analysis confirm the above mentioned left- and right-hand terminations (Fig. 2J).

In the Late Stage the main surface faults increase their length, both by linkage and lateral propagation (Fig. 2k, 2l). Other small faults also grow near their lateral tips. Hanging wall subsidence remains symmetric and bounded by main faults. The D.I.C. analysis shows that the decoupled area broadens following the new fault segments (Fig. 2m). The area where the strike-parallel component of displacement is seen (Fig. 2n) is nearly the

same as that observed in the previous stage. The largest strain occurs along the main faults, especially along segments in correspondence with the master fault at depth (Fig. 2o). The peaks of vertical displacement along the two main fault traces remains in the same position as in the previous stage (Fig. 3a). Finally, the cumulative displacement profile peaks near the central part of the fault system and is rather symmetric (Fig. 3c).

The other two isotropic experiments, i.e. E1B and E1C, show similar results to the E1A both in terms of the evolution of surface faults and in terms of distribution of vertical displacement (Fig. 3c).

3.2. Experiments with a precut

3.2.1. Synthetic-attitude precuts (E2, 30°; E3, 45°; E4, 60°)

Figures 5, 6, and 7 show the results of the experiments with a synthetic precut. We use the reference stages Early, Middle and Late for the description of the experiments.

During the Early Stage of E2 the precut is reactivated along the most part of its trace and no bending-moment faults develop along the vertical projection of the master fault (Fig. 5a). Conversely, in E3 the precut is not reactivated and bending-moment faults appear (Fig. 5b), although they are not as well developed as in the isotropic experiments (e.g., Fig. 2b). In E4 the precut is reactivated only in the hanging wall of the master fault and bending-moment faults appear (Fig. 5c). The hanging wall subsidence is rather symmetric in E3 and asymmetric in E2 and E4. In these latter cases, the lowermost subsiding area coincides with the segment of the reactivated precut. The D.I.C. analysis shows that the horizontal displacement field in E2 is strongly influenced by the activity of the precut, enhanced in the hanging wall and inhibited in the footwall (Fig. 6a). The active role of the precut is lesser in the other two experiments (Figs. 6b, and 6c), and the distribution of displacement is similar to that observed in the isotropic experiment (Fig. 2c). The reactivation of the precut in E2 displays a bimodal, asymmetric distribution with a minimum value located where the precut trace intersects the buried tip of the master fault (Fig. 7a). In E3 and E4 the peaks of the displacement distribution along the precut are present only on the right-hand side of the ROI (Figs. 7c and 7e).

In the Middle Stage new faults form in all three experiments and the precut continues to be reactivated. In E2 new faults form on either side of the precut, although those on the left are more developed (Fig. 5d). In E3 a new fault develops on the left of the precut and only minor faults or bending-moment faults are visible on its right (Fig. 5e). In E4 newly-formed faults are similar to those observed in E3, but those on the left of the precut are more developed (Fig. 5f). Precuts are reactivated in all three experiments, and preferably in the hanging wall of the newly-formed faults. The subsidence areas appear asymmetric and their lowermost point coincides with the reactivated portion of the precut (Figs. 5d-5f). In E2 the strike-parallel component of the horizontal displacement begins to be confined in the triangular area between the precut and newly-formed faults (Fig. 6d). The same occurs in E3 and E4, although with less pronounced effects than in E2 (Figs. 6e, and 6f). The displacement distribution of newly-formed faults in E2 is bimodal and asymmetric with two peaks located on the left and right sides of the precut, left- and right-skewed, respectively (Fig. 7b). The precut reactivation profile in E2 is symmetric on the left-hand side and left-skewed on the other side (Fig. 7a). In E3 and E4 the precut reactivation profile has a similar shape as those of the Early Stage with peaks near the clay-box wall (Figs. 7c, and 7e). Conversely, the newly-formed fault both in E3 and E4 show asymmetric, left-skewed profiles, although the E3 profile is also bimodal (Figs. 7d-7f).

In the Late Stage the newly-formed faults show a weak lateral propagation (Figs. 5g-i), except for those to the right of the precut in E2. The shape of the subsidence areas suggests that the increase of vertical displacement of newly-formed faults and the reactivation of precuts in their hanging wall is the dominant mechanism. In E2 a small subsiding area is located in the area between the precut and newly-formed faults (Fig. 5g). In E3 and E4 a weak lateral propagation of newly-formed faults is visible where they intersect the precut (Figs. 5h-i). The evolution of the displacement field is similar to that of the Middle Stage (Figs. 6g-6i). The displacement distribution in E2 continues to be bimodal and asymmetric both for the precut reactivation (Fig. 7a) and for newly-formed faults (Fig. 7b). The two displacement peaks of newly-formed faults are both located near the lateral tips of the master fault, one right skewed and one left skewed. Conversely, both sides of the precut reactivation are left skewed. The precut reactivation trend is maintained in E3 and E4 (Figs. 7c, and 7e),

but the displacement distribution of newly-formed faults is different. In E3 the displacement distribution tends to be rather flat topped and continuous (Fig. 7d), whereas in E2 and E4 it is split across the intersection with the precut and peaked on either sides (Figs. 7b, and 7f).

3.2.2. Antithetic-attitude precuts (E5, 30°; E6, 45°; E7, 60°)

Figures 8, 9, and 10 show the results of the experiments with an antithetic precut. We use the reference stages Early, Middle and Late for the description of the experiments.

During the Early Stage, bending-moment faults form only in E7. The precut appears reactivated in different parts in the three experiments: only the central part in E5, the right-hand half in E6, and the right-hand portion in E7 (Figs. 8a-8c). The subsiding area is asymmetric in all three experiments and exhibits a different pattern across the surface trace of the precut (Figs. 8a-8c). This asymmetry is also evident from the D.I.C. analysis (Fig. 9). The horizontal surface displacement is inhibited in the triangular area between the precut and the vertical projection of the master fault in the footwall and slightly enhanced in the hanging wall of the master fault (Figs. 9a-9c). In E7 this effect is less pronounced (Fig. 9c).

In the Middle Stage, bending-moment faults and new faults form, some of the latter with noticeable vertical displacement (Figs. 8d-8f, and 10b). The precut does not show significant activity in E5, whereas its activity is more pronounced in E6 and E7 (Figs. 8e-8f). The D.I.C. analysis shows a rather symmetric displacement in E5 and strongly asymmetric displacement in E6 and E7 because smaller displacement occurs in the triangular area between the precut and the vertical projection of the master fault (Figs 9d-9f). In E7 the displacement in the hanging wall of the master fault is significantly enhanced (Fig. 9f). Similarly to the Early Stage, the reactivation of the precut is limited (Figs. 10a-10c). The displacement on newly-formed faults in E5 appears to have three peaks, progressively larger from left to right (Fig. 10 b) and thereby determining a strong right skew of the overall profile. In E6 the distribution is bimodal, with the two peaks having much smaller maximum values than in E5 (Fig. 10d). In E7 the distribution of the displacement appears unimodal and rather symmetric (Fig. 10f).

In the Late Stage newly-formed faults increase their length in all experiments (Figs. 8g-8i), mainly across the precut showing a few distinctive structural features: a small graben in E5 (Fig. 8g) and a left-stepped segment in E7 (Fig. 8i). In all experiments, only the portion of the precut located in the hanging wall of the master fault is activated (Figs. 8g-8i). The surface displacement is quite symmetric in E5, quite asymmetric in E6, and clearly asymmetric in E7 (Figs. 9g-9i). In E5 and E6 the displacement vectors located between newly-formed faults and precuts are perpendicular to the strike of the precut themselves, whereas in E7 they form an acute angle with the precut strike. The vertical displacement along precuts increases in the portion located on the master fault hanging wall (Figs. 10a, 10c, 10e) and is more pronounced in E5. The displacement distribution along newly-formed faults is bimodal in E5 and E6; unimodal and quite uniform in E7 (Figs. 10b, 10d, and 10f). The two bimodal distributions have their peaks separated by a minimum near the intersection with the precut.

4. DISCUSSION

Model results show that precuts - the analogue of pre-existing discontinuities - affect all parameters associated with the development of new normal faults. The extent of this influence depends largely on the orientation of the precut with respect to the strike of the newly-forming faults. Among the several features we described in previous sections, in the following we quantitatively discuss only those related to the on-fault deformation because they are simpler to be measured in the field and are the most commonly used to describe the characteristics of extensional systems. As regards the off-fault features (e.g., accommodation space, displacement field), although they could be quantified in our experiments, they are not easily quantifiable in nature. For instance, to quantify the accommodation space in a natural case, three-dimensional seismic data is necessary.

The parameters that we use to describe on-fault deformation are: the displacement distribution, the value and the position of maximum displacement (Dmax), and the surface trace length (L). We also analyze the fault segmentation and discuss the relationship between Dmax and L. In the next sections we first derive a

model of fault development from the isotropic experiment, and then compare such model with results of experiments with precut to quantify the departures induced by the precut. Finally, we make a qualitative comparison between our observations and two natural cases in two quite different tectonic settings.

4.1. Isotropic experiments

There exists a general consensus that an isolated fault grows in such a way that its surface displacement has a maximum in the center and decreases to zero toward both ends. Conversely, the expected shape of the displacement distribution is still the object of debate. For instance, existing models propose various shapes of normalized-displacement profiles, such as linear, circular, elliptical, bell-like, or even more complex shapes (e.g. Pollard and Segall, 1987; Walsh and Watterson, 1987; Bürgmann et al., 1994; Peacock and Sanderson, 1996; Manighetti et al., 2001; Scholz, 2002; Schlagenhauf et al., 2008). We may consider the linear and the circular models as end members of this set of distributions because they generally encompass all the others. To compare our results with these existing models we first obtain a Gaussian fit of the displacement point data taken at several distances along the traces of newly-formed faults in the three isotropic experiments, both for the Middle Stage and Late Stage (Fig. 11; data and details of the Gaussian fit are reported in Appendix). Then, we measure the departures between the experimental results and the Gaussian, circular, and linear models for normalized profiles and calculate the root mean square (RMS) of these deviations (Figs. 11b-11c). The Gaussian model always shows the best performance (lowest RMS), indicating that this shape is more appropriate than either the circular or linear models. Conversely, the circular model always exhibits the worst performance (highest RMS), although it improves with increasing displacement (Late Stage). The performance of the linear model, instead, worsens with increasing displacement. In other words, the RMS separation between the Gaussian and linear models increases with increasing displacement on the master fault (from Middle to Late Stage), whereas the RMS separation between the Gaussian and the circular models decreases. In simple statistical terms, this implies that the linear model, though worse than the Gaussian, can still be appropriate to describe the early phases of fault development. Notice also that the Gaussian curve takes different shapes,

from a more to a less peaked form, as the fault progresses from the Middle to the Late Stage (Fig. 11a). From a mechanical viewpoint, this is indicative of different growing phases in which the fault length rapidly increases in the early stage and then remains constant while displacement accumulates. Such results are reminiscent of the "constant length model" proposed by Walsh et al. (2002).

4.2. Comparison between isotropic experiments and experiments with precuts

Below we discuss differences between the isotropic experiment and experiments with precuts in terms of displacement distribution, Dmax value and position along the profile, fault length, Dmax/L ratio, and fault segmentation. Table 1 provides a synoptic view of the several cases analyzed for the Middle and Late Stages of fault development in our experiments. In this table we propose a quantitative estimate of the percent variation of fault parameters in experiments with precut relative to the same parameter in the isotropic case.

4.2.1 Cumulative displacement distribution

Figure 12a shows the cumulative displacement profiles of all experiments with precut (data in Appendix). As mentioned in the previous section, the experiments with a precut show different surface fault profiles in terms of displacement amount and distribution. The analysis concerns a comparison between cumulative displacement of the isotropic experiment and each experiment with a precut, separately for the Middle and Late Stages. This analysis is aimed at answering the following question: does a precut induce statistically significant departures from the ideal surface fault profile in the isotropic case?

Figure 12b shows that many data points of the experimental profiles of faults affected by a precut fall outside the 95% prediction interval (PI95) of the Gaussian profiles. This occurrence confirms that the presence of the precut induces modifications of the surface fault profiles that exceed the aleatory fluctuations in isotropic conditions (with 95% likelihood). The RMS of these deviations, separately calculated for the side of the experimental box without precuts, for the side with precuts, and for both sides (Figs 12b, and 12c), shows that:

1) The RMS of E7 is similar to that of E1, so that the effect of the precut in this case cannot be discriminated from the case of the isotropic case; in all other cases the side with precut (right) exhibits an RMS significantly larger than that of the side without precut (left);
2) The RMS of either left or right side and that of both sides of all experiments with precut is always larger than that of E1 and E7;
3) The precuts seems to affect the profiles significantly; this effect is so pervasive that even the RMS of the left-hand side is higher than that of E1 and E7;
4) E2 and E6 seem to be the precut configurations that affect the most the surface fault profiles in both the Middle and Late Stages, though relatively less for E6 in the Late Stage;
5) E3, E4, and E5 exhibit rather similar RMS to one another in both stages.

To summarize the departures of the cumulative displacement in the experiments with precut with respect to the isotropic case, we quantify the percent influence comparing the equivalent total area below the displacement profiles. This value is calculated as

$$R = |V_{En} - V_{E1}|/V_{E1} \quad (2)$$

where R is the percent ratio, V_{En} is the parameter value of the relevant experiment n (2-7), and V_{E1} is the parameter value in E1 (Table 1). The results show that in the Middle Stage, the largest departures are those of E2, and E6. Significant deviations are shown also for the displacement of E4. Conversely, E3, E5, and E7 do not exhibit significant deviations. In the Late Stage, values of E2 and E6 are still those showing the largest deviations, but they slightly reduce the percent value. Also E4 show the same downward trend. Conversely, E3, E5, and E7 increase their deviations.

4.2.2. Dmax

The Dmax of the fault profiles can be seen from two viewpoints: 1) its absolute value and 2) its position along the profile. To evaluate differences and similarities between experiments with a precut and the isotropic experiment, we use the Dmax of the Gaussian fit and PI95 of the isotropic experiment.

It should be stressed that in all experiments we impose a uniform displacement onto the master normal fault at depth. This implies that the Dmax is expected to fall near the center of the displacement profile unless some disturbance is introduced. Notice that the location of Dmax for the isotropic experiments is not exactly in the center (Fig. 12e) but lies slightly to the right-hand side in both the Middle and Late Stages. We consider this departure from the ideal distribution as due to aleatory variability resulting from various experimental reasons, including unwanted imperfections in the construction of the apparatus and in the deployment of the clay body. Despite the possible albeit minimal aleatory departures, we observe that the Dmax can be found at various significant distances on either side in different experiments with a precut (Fig. 12e). It may also shift from left to right or vice versa, or it may remain stable while the fault progresses from the Middle to the Late Stage. In few cases the Dmax can even be found to the right of the precut intersection. Notice also that few distributions are bimodal.

The percent influence of the Dmax position along the profile is calculated as the ratio between the horizontal offset and the half fault length in E1 (Table 1). For the Dmax value, the percent influence is calculated using eq. (2). In the Middle Stage, both Dmax value and position in E3, E4, and E7 do not show significant departures with respect to E1. The departures appear quite significant in E5. E2 shows a large departure as regards the Dmax position, although its Dmax value is not so different with respect to E1. In E5 both the position and the value of Dmax substantially deviate with respect to E1. In E6, only the Dmax value show large deviations. In the Late Stage only E6 maintains large deviation both in the value and position of Dmax. Other experiments do not show significant deviation, although with specific percentages. The exception is the Dmax position in E2 that maintains a large deviation.

4.2.3. Length

The fault length is measured as the shortest distance between the farthest end points (Fig. 12f). In general the departure from the fault length in isotropic conditions is larger in the Middle Stage than in the Late Stage (Table 1). Also in this case, the percent influence is calculated using eq. (2).

In the Middle Stage, the experiment with a larger deviation is E2 because most of the brittle deformation occurs through the reactivation of the precut. Significant departures are noticeable also in E4, and E6. Progressively smaller deviations are found in E3, E5, and E7, and this decrease seems partially related to the amount of precut reactivation in these experiments. In the Late Stage only E6 maintains a noticeable deviation with respect to E1.

4.2.4. Dmax/L

Having just examined both Dmax and L in our experiments, it is worth making a brief note about their relationship. The Dmax/L ratio spans several orders of magnitude (Schlische et al., 1996; Kim and Sanderson, 2005; Grasemann et al., 2011; Torabi and Berg, 2011) and it is often used for exploring geometry statistics of faults in various tectonic settings, host-rock types, and faulting processes. Due to several objective experimental difficulties, however, Dmax and L observations are usually affected by large measurement uncertainties (Kim and Sanderson, 2005). When actual data are plotted on a Dmax versus L diagram the scatter is thus evident, especially for single datasets. We take advantage of the controlled environment of our experiments to analyze this relationship. Figure 13 shows that our Dmax/L data cluster very close to the fitting line for normal faults reported by Kim and Sanderson (2005). On the one hand, this demonstrates that the normal faults of our wet-clay models share the same scale-invariant properties with several types of natural faults. On the other hand, we notice that our data exhibit only minimal scatter suggesting that the Dmax/L ratio is not very sensitive to the presence or absence of precuts. The same may thus apply for natural normal faults that develop in the presence of pre-existing discontinuities. Nonetheless, Middle Stage and Late Stage faults form two clear subclusters separated along the Dmax axis. This implies that while these faults grow, the rate of Dmax increase is relatively faster than the rate of L lateral increase. This reflects the irregular increments of length and displacement that are typical of this process in our experiments, as already observed both in other analogue models (Mansfield and Cartwright, 2001) and in natural datasets (Walsh et al., 2002).

4.2.5. Apparent segmentation

With the term “apparent segmentation”, we refer to a situation where surface displacement distribution of a new fault shows multiple peaks and local minima in between that do not correspond to a real change in the displacement along the master fault at depth.

To evaluate the apparent segmentation we look at the modes of the displacement distribution in normalized profiles and identify the two largest modes among all peaks, as well as the antimode in between. Then we calculate the mean amplitude (vertical separation between the mean of the peak-to-peak distance of major modes and the antimode). Finally, we estimate the influence of precuts as the percent ratio between the mean amplitude and the mean of the modes.

Our calculations for the Middle Stage show that E2, E4, and E6 are not only bimodal but also have large deviations with respect to E1. E5 and E7 also show significant deviations, although the difference between peaks and minima is smaller than those of the previous cases. E3 is the experiment with the lowest deviation with respect to E1 and show no signs of apparent segmentation. In the Late Stage, the apparent segmentation value decreases in most experiments, thereby indicating that when the new faults reach a mature stage in their surface development, the effect of the precut onto the apparent segmentation tends to diminish.

4.3. Comparison of experimental results with natural cases

The superposition of differently oriented extensional faults may occur in two independent instances: in multiphase rift areas if the direction of extension is different during each rift phase, and in orogenic belts where both the pre- and post-contractional tectonic regimes are characterized by extension. Although both cases are intrinsically complex to study, the second case is more complex because two kinds of structures may affect the evolution of the youngest extensional faults; the oldest extensional faults and the subsequent thrust faults.

Multiphase rifts with non-coaxial tension stress fields have been described in many regions from around the world, including the African Rift (Bonini et al., 2007), the Gulf of Thailand (Morley et al., 2004),

Alaska (Nixon et al., 2014), and the North Sea (Whipp et al., 2014). A diachronic and non-coaxial rift in the North Sea, the Horda Platform to the east of the Viking Graben (Figs. 14a and 14b), was the object of a recent study by Duffy et al. (2015) that investigated the role of a Late Permian-to-Early Triassic extensional fault system (first rift phase) on the evolution of Late Jurassic-to-Early Cretaceous normal faults (second rift phase). In particular, Duffy et al. (2015) used an integrated 3D dataset of seismic reflection lines and borehole logs to analyze in detail how the N-S-trending Tusse Fault, that was active during the first rift phase, affected the growth of new NW-SE-trending faults formed during the second rift phase. Some of the various fault interaction styles are reminiscent of our experimental results. The second (younger) set of faults formed at different strike angles and opposite attitude (antithetic or synthetic) with respect to the first (older) Tusse Faults (Fig. 14b), in a similar configuration to that of E3 and, secondarily, in E6 (Fig. 4). Duffy et al. (2015) suggested that: 1) the nucleation of the second set of faults occurred near or close to the pre-existing fault; 2) when a fault of the second set interacted with the Tusse Fault, the throw and accommodation space of the latter increased; 3) the Tusse Fault acted as a mechanical barrier to the lateral propagation of faults of the second set. These observations are very similar to some features predicted by our experiments, such as those that can be seen in Fig. 5b for case 1) with new faults nucleating near the precut in the early stage; in Fig. 7c for case 2) where the displacement and the accommodation space is larger near the precut; and Fig. 7d for case 3) in which the lateral propagation of the new faults is strongly obstructed by the precut giving rise to an asymmetric displacement profile.

Post-orogenic extension is another frequent case of fault interactions that has already been described in several regions of the world, such as the Basin and Range of USA and Mexico (e.g. Wernicke, 1981; Malavieille, 1993), the Taiwanese Orogen (Teng, 1996), and the Apennines in Italy (Elter et al., 1975), just to name a few cases. The central Apennines, in particular, exhibits a remarkably complex tectonic setting resulting from the overprinting of successive tectonic phases (Figs. 14c and 14d): from Mesozoic rifting to Neogene contraction followed by Plio-Quaternary extension (e.g. Calamita et al., 2011). Extension is also the main driver of the significant seismogenic potential of this region; therefore, the study of the younger faults is crucial,

tough especially difficult because of their interactions with older faults (Bonini et al., 2014). The Fucino Basin exemplifies this situation since it is the locus of one of the largest earthquakes of the region, the M_w 7 earthquake of 13 January 1915 (Rovida et al., 2011) which ruptured a 30-km-long, NW-SE-striking normal fault (e.g. Ward and Valensise, 1989). The Fucino Basin is a large intermountain basin filled in by Plio-Quaternary lacustrine sediments, which being especially sensitive to the evolution of the accommodation space through time recorded a long history of fault interactions (Fig. 14e; Cavinato et al., 2002). The interaction between the NW-SE-trending Fucino Fault and the NNE-SSW-trending Tre Monti Fault compares well with the setting of E4 (Fig. 4). In this experiment, during the early stage of extension the accommodation space is mainly created in the area where the younger normal faults interfere with the precut. During the middle and late stages, as displacement increases on both fault system (Figs. 7e and 7f), the accommodation space enlarges and its deepest part migrates toward the middle of the master fault. The evolution of the accommodation space in our model results can be recognized in the Fucino Basin infill evolution reconstructed by Cavinato et al. (2002) on the basis of seismic reflection lines, borehole logs, and exposed stratigraphy of lacustrine sediments. In Cavinato et al.'s reconstruction the Upper Pliocene infill has a depocenter in the northern corner of the basin, toward the intersection between the Fucino Fault and the Tre Monti Fault. Successively, throughout the Pleistocene and Holocene, the basin infill enlarges and its depocenter deepens toward the northeast. As the younger Fucino Fault evolves, it offsets the Quaternary deposits and leaves uplifted terraces on its footwall.

Despite the two natural cases illustrated above developed in very different geological times and tectonic settings, they find a faithful analogue in our experiments. These two examples, however, were well documented through expensive and time-consuming investigations (seismic lines and borehole logs) which are not necessarily available everywhere. We thus suggest the results from our experiments can be used as proxies or for the preliminary assessment fault interaction behavior and for reinterpreting tectonic studies that could not take into account the fault interaction with pre-existing structures.

5. CONCLUSIONS

We investigated how pre-existing discontinuities affect the surface expression of an initially-blind, isolated master normal fault. To this end we used analogue models built by introducing a precut - i.e. a mechanical discontinuity - into a clay (wet kaolin) layer placed on top of the master fault. Using this configuration we carried out six experiments where the discontinuity could have both a synthetic or antithetic attitude and was preset at angles of 30°, 45°, and 60° with respect to the strike of the master fault. The results of these experiments were then compared with those from a preparatory experiment carried out without inserting any discontinuity (isotropic reference model). All other conditions were identical for all seven experiments.

Our experimental results suggest that the presence of a discontinuity exerts significant, though very variable, control on several parameters that are commonly adopted to describe the geometry and behavior of natural normal faults (Table 1). In general, this control decreases as the new fault progresses toward a more mature development stage, but the actual control at each stage strongly depends on the angle at which the pre-existing discontinuities intersect the new faults. For instance, pre-existing discontinuities with synthetic attitude and small angle (≤45°) of intersection induce significant departures of the value of several parameters with respect to what is generally expected from an isolated fault growing in a mechanically isotropic setting. Conversely, more moderate departures are induced by synthetic attitude discontinuities with higher angle (≥45°) of intersection, or by antithetic attitude discontinuities with small angle (≤45°) of intersection. Our findings also show that despite both Dmax and L are variously affected by the presence of a precut, the Dmax/L ratio is generally insensitive to it. This does not mean that the Dmax/L ratio is a poor descriptor of faults in general but that it may be a poor predictor of the presence/absence of the complexities in fault evolution analyzed here. In more practical terms, we notice that when a single observable is considered, the amount of departure induced by each type of precut is extremely variable from case to case and it is not easily predictable. We thus suggest that multiple observables be taken into consideration in the analysis of normal faults in the presence of pre-existing discontinuities.

In summary, our findings may improve our understanding of how normal faults evolve in the presence of structures inherited from previous tectonic phases, especially in studies of active faulting where the geometry and behavior of faults are commonly inferred from surface data. No matter how challenging this inference may seem, the obvious reason behind this strategy is that surface data are more accessible and cost-effective than subsurface data. This type of inference is especially needed, and thus often applied, in large collections of earthquake fault data oriented at seismic hazard analysis (Haller and Basili, 2011; Christophersen et al., 2015) which requires that empirical relationships or theoretical interpretative models be applied. In many active tectonic environments, however, faults are not isolated and the application of empirical or theoretical models can be challenging or lead to biases. Unlike field data, the controlled environment of our study provided an opportunity to evaluate the surface expression of an isolated normal fault whose geometry and kinematic properties at depth - as well as the geometry of the imposed disturbance (e.g. the precut) - are accurately known. Although the natural context is much more complex than our models, we have found a good correspondence between our findings and two natural cases (the Viking Graben in the North Sea and the Fucino Basin in the Apennines) for which good field data are available. We thus suggest that our first attempt at ranking the influence of the precut onto several observables that are commonly adopted to characterize surface faults can be used as a guidance tool for aiding the interpretation of natural normal faults that develop in the presence of pre-existing discontinuities.

ACKNOWLEDGMENTS

All experiments were carried out at the 3D Modelling Laboratory at University of Pavia. The work was supported by Project “Abruzzo” (code: RBAP10ZC8K_003) funded by the Italian Ministry of Education, University and Research (MIUR), and by the “Finanziamenti di Ateneo per progetti scientifici – FRA 2013, P.I. Gian Andrea Pini” allocated by Università di Trieste, which are both gratefully acknowledged. Midland Valley

Ltd is thanked for making available the Move software to the University of Trieste and to the University of Pavia (ASI –Academic Software Initiative).

REFERENCES

Ahmad, M.I., Dubey, A.K., Toscani, G., Bonini, L., Seno, S., 2014. Kinematic evolution of thrust wedge and erratic line length balancing: insights from deformed sandbox models. International Journal of Earth Sciences, 103, 1, 329-347, doi: 10.1007/s00531-013-0947-8.

Arch, J., Maltman, A.J., Knipe, R.J., 1988. Shear-zone geometries in experimentally deformed clays: the influence of water content, strain rate and primary fabric. Journal of Structural Geology, 10 (1), 91-99, doi: 10.1016/0191-8141(88)90131-9.

Byerlee, J., 1978. Friction of rocks. Pure and Applied Geophysics 116, 615–626.

Bonini L., Basili R., Toscani G., Burrato P., Seno S., Valensise G., 2015. The role of pre-existing discontinuities in the development of extensional faults: an analog modeling perspective. Journal of Structural Geology, 74, 145-158, doi:10.1016/j.jsg.2015.03.004.

Bonini, L., Dallagiovanna, G., Seno, S., 2010. The role of pre-existing faults in the structural evolution of thrust systems: insights from Ligurian Alps (Italy). Tectonophysics, 480, 73-87. doi:10.1016/j.tecto.2009.09.021

Bonini, L., Di Bucci, D., Toscani, G., Seno, S., Valensise, G., 2011. Reconciling deep seismogenic and shallow active faults through analogue modelling: the case of Messina Straits (southern Italy). Journal of the Geological Society, 168 (1), 191-199. doi:10.1144/0016-76492010-055.

Bonini, L., Di Bucci, D., Toscani, G., Seno, S., Valensise, G., 2014. On the complexity of surface ruptures during normal faulting earthquakes: excerpts from the 6 April 2009 L'Aquila (central Italy) earthquake (Mw 6.3). Solid Earth, 5, 389-408, doi: 10.5194/se-5-389-2014.

Bonini, M., 1998. Chronology of deformation and analogue modelling of the Plio-Pleistocene 'Tiber Basin': implications for the evolution of the Northern Apennines (Italy). Tectonophysics 285, 147–165.

Bonini, M., Souriot, T., Boccaletti, M., Brun, J.P., 2007. Successive orthogonal and oblique extension episodes in a rift zone: laboratory experiments with application to the Ethiopian Rift. Tectonics 16 (2), 347-362.

Bonini, M., Sani, F., Antonielli, B., 2012. Basin inversion and contractional reactivation of inherited normal faults: A review based on previous and new experimental models. Tectonophysics 522–523 (2012) 55–88.

Bürgmann, R., Pollard, D.D., Martel, S.J., 1994. Slip distributions on faults: effects of stress gradients, inelastic deformation, heterogeneous host-rock stiffness, and fault interaction. Journal of Structural Geology 16, 1675– 1690.

Calamita, F., Satolli, S., Scisciani, V., Esestime, P., Pace, P., 2011. Contrasting styles of fault reactivation in curved orogenic belts: Examples from the Central Apennines (Italy). Geol. Soc. Am. Bull., 123, 1097–1111.

Cerca, M., Ferrari, L., Corti, G., Bonini, M., Manetti, P., 2010. Analogue model of inversion tectonics explaining the structural diversity of Late Cretaceous shortening in southwestern Mexico. Lithosphere 2, 172–187.

Christophersen, A., Litchfield N., Berryman K., Thomas R., Basili R., Wallace L., Ries W., Hayes G., Haller K.M., Toshikazu Y., Koehler R.D., Clark D., Wolfson-Schwehr M., Boettcher M.S., Villamor P., Horspool N., Ornthammarath T., Zuñiga R., Langridge R.M., Stirling M.W., Goded T., Costa C., Yeats R., 2015. Development of the Global Earthquake Model's neotectonic fault database. Natural Hazards, under revision.

Collettini, C., Sibson, R.H., 2001. Normal faults, normal friction? Geology, 29(10), 927-930, doi: 10.1130/0091-7613.

Cooke, M.L., Schottenfeld, M.T., Buchanan, S.W. 2013. Evolution of fault efficiency at restraining bends within wet kaolin analog experiments. Journal of Structural Geology 51, 180-192.

Cooke, M.L., van der Elst, N.J., 2012. Rheologic testing of wet kaolin reveals frictional and bi-viscous behavior typical of crustal materials. Geophysical Research Letters, 39, http://dx.doi.org/10.1029/2011GL050186.

Corti, G., van Wijk, J., Cloetingh, S., Morley, C.K., 2007. Tectonic inheritance and continental rift architecture: numerical and analogue models of the East African Rift system. Tectonics 26, TC6006.

Cowie, P.A., Shipton, Z., 1998. Fault tip displacement gradients and process zone dimensions. Journal of Structural Geology 20, 983–997.

Dawers, N.H., Anders, M.H., Scholz, C.H., 1993. Growth of normal faults: displacement–length scaling. Geology 21, 1107– 1110.

Decarlis, A., Maino, M., Dallagiovanna, G., Lualdi, A., Masini, E., Seno, S. 2013. Salt tectonics in the SW Alps (Italy–France): From rifting to the inversion of the European continental margin in a context of oblique convergence. Tectonophysics 636, 293-314.

Del Ventisette, C., Montanari, D., Bonini, M., Sani, F., 2005. Positive fault inversion triggering 'intrusive diapirism': an analogue modelling perspective. Terra Nova 17, 478–485.

Del Ventisette, C., Montanari, D., Sani, F., Bonini, M., 2006. Basin inversion and fault reactivation in laboratory experiments. In: Tavarnelli, E., Butler, R., Grasso, M. (Eds.), Tectonic Inversion Processes and Structural Inheritance in Mountain Belts: Journal of Structural Geology, 28, pp. 2067–2083.

Di Domenica, A., Bonini, L., Calamita, F., Toscani, G., Galuppo, C., Seno, S., 2014. Analogue modeling of positive inversion tectonics along differently oriented pre-thrusting normal faults: an application to the Central-Northern Apennines of Italy. Bull. Geol. Soc. Am., 126, 943e955. http://dx.doi.org/10.1130/B31001.1.

Dubois, A., Odonne, F., Massonnat, G., Lebourg, T., Fabre, R., 2002. Analogue modelling of fault reactivation: tectonic inversion and oblique remobilisation of grabens. Journal of Structural Geology 24, 1741–1752.

Duffy, O.B., Bell, R.E., Jackson, C.A-L., Gawthorpe, R.L., Whipp, P.S., 2015. Fault growth and interactions in a multiphase rift fault network: Horda Platform, Norwegian North Sea. Journal of Structural Geology, 80, 99-119.

Eisenstadt, G., Sims, D., 2005. Evaluating sand and clay models; do rheological differences matter? Journal of Structural Geology, 27, 1399–1412, 2005.

Elter, P., Giglia, G., Tongiorgi, M., Trevisan, L., 1975. Tensional and compressional areas in the recent (Tortonian to present) evolution of the Northern Apennines. Boll. Geofis. Teor. Appl., 42, 3-18.

Faccenna, C., Nalpas, T., Brun, J.-P., Davy, P., Bosi, V., 1995. The influence of pre-existing thrust faults on normal fault geometry in nature and in experiments. Journal of Structural Geology, 17 (8), 1139-1149, doi: 10.1016/0191-8141(95)00008-2

Garcia, D., 2011. A fast all-in-one method for automated post-processing of PIV data. Experiments in Fluids, 50(5), 1247-1259.

Gartrell, A., Hudson, C., Evans, B., 2005. The influence of basement faults during extension and oblique inversion of the Makassar Straits rift system: insights from analog models. AAPG Bulletin 89, 495–506.

Gawthorpe, R.L., Leeder, M.R., 2000. Tectono-sedimentary evolution of active extensional basins. Basin Research, 12, 195–218.

Grasemann, B., Exner, U., Tschegg, C., 2011. Displacement-length scaling of brittle faults in ductile shear Journal of Structural Geology, 33 (11), 1650-1661. doi:10.1016/j.jsg.2011.08.008

Haller, K.M., Basili, R., 2011. Developing seismogenic source models based on geologic fault data. Seismological Research Letters, 82, 519-525, doi:10.1785/gssrl.82.4.519.

Handin, 1966. Strength and ductility. In: Clark, S.P. (Ed.), Handbook of Physical Constants, 97. Geological Society of America Memoir, pp. 233–289.

Hatem, A.E., Cooke, M.L., Madden, E.H., 2015. Evolving efficiency of restraining bends within wet kaolin analog experiments. Journal of Geophysical Research B: Solid Earth, 120 (3), pp. 1975-1992.

Henza, A., Withjack, M.O., Schlische, R.W., 2010. Normal-fault development during two phases of non-coaxial extension: An experimental study, J. Struct. Geol., 32, 1656–1667, doi:10.1016/j.jsg.2009.07.007.

Hubbert, M.K., 1937. Theory of scale models as applied to the study of geologic structures. Geological Society of America Bulletin, 48, 1459–1520.

Hyppolite, J.-C., Angelier, J., Roure, F., 1994. A major geodynamic change revealed by Quaternary stress patterns in the Southern Apennines (Italy). Tectonophysics, 230, 199–210.

Jackson, J.A., White, N.J., 1989. Normal faulting in upper continental crust: observations from regions of active extension. Journal of Structural Geology, 11, 15-36.

Kim, Y-.S., Sanderson, D.J., 2005. The relationship between displacement and length of faults: a review. Earth-Science Reviews, 68, 317–334.

Konstantinovskaya, E.A., Harris, L.B., Poulin, J., Ivanov, G.M., 2007. Transfer zones and fault reactivation in inverted rift basins: insights from physical modelling. Tectonophysics, 441, 1–26.

Krantz, R.W., 1988. Multiple fault sets and three-dimensional strain. Journal of Structural Geology 10, 225–237.

Lezzar, K.E., Tiercelin, J.-J., Le Turdu, C., Cohen, A.S., Reynolds, D.J., Le Gall, B., Scholz, C.A., 2002. Control of normal fault interaction on the distribution of major Neogene sedimentary depocenters, Lake Tanganyika, East African rift. AAPG Bull., 86, 1027–1060.

Leonard, M., 2014. Self-Consistent Earthquake Fault-Scaling Relations: Update and Extension to Stable Continental Strike-Slip Faults. Bulletin of the Seismological Society of America, doi: 10.1785/0120140087.

Malavieille, J., 1993. Late orogenic extension in mountain belts: insights from the Basin and Range and the Late Paleozoic Variscan Belt. Tectonics, 12, 5, 1115-1130.

Mandl, G., 2000. Faulting in brittle rocks: an introduction to the mechanics of tectonic faults, Springer Berlin.

Manighetti, I., King, G.C.P., Gaudemer, Y., Scholz, C.H., Doubre, C., 2001. Slip accumulation and lateral propagation of active normal faults in Afar. Journal of Geophysical Research 106, 13667-13696.

Mansfield, C., Cartwright, J., 2001. Fault growth by linkage: observations and implications from analogue models. Journal of Structural Geology, 23, 745–763.

Marques, F.O., Nogueira, C.R., 2008. Normal fault inversion by orthogonal compression Sandbox experiments with weak faults. Journal of Structural Geology 30, 761–766.

McClay, K.R., 1989. Analogue models of inversion tectonics. In: Cooper, M.A., Williams, G.D. (Eds.), Inversion tectonics, 44. Geological Society of London, Special Publication, 41–62.

McClay, K.R., Dooley, T., Ferguson, A., Poblet, J., 2000. Tectonic evolution of the Sanga Sanga Block, Mahakam Delta, Kalimantan, Indonesia. AAPG Bulletin, 84, 765–786.

Morley, C.K., Haranya, C., Phoosongsee, W., Pongwapee, S., Kornsawan, A., Wonganan, N., 2004. Activation of rift oblique and rift parallel pre-existing fabrics during extension and their effect on deformation style: examples from the rifts of Thailand. Journal of Structural Geology, 26, 1803-1829.

Muraoka, H., Kamata, H., 1983. Displacement distribution along minor fault traces. Journal of Structural Geology 5, 483–495.

Nicol, A., Watterson, J., Walsh, J.J., Childs, C., 1996. The shapes, major axis orientations and displacement patterns of fault surfaces. Journal of Structural Geology, 18, 235- 248.

Opheim, J.A., Gudmundsson, A., 1989. Formation and geometry of fractures, and related volcanism, of the Krafla fissure swarm, northeast Iceland. Geological Society of America Bulletin 101, 1608– 1622.

Paton, D.A., 2006. Influence of crustal heterogeneity on normal fault dimensions and evolution: southern South Africa extensional system. Journal of Structural Geology, 28, 868-886.

Peacock, D.C.P., Sanderson, D.J., 1991. Displacement and segment linkage and relay ramps in normal fault zones. Journal of Structural Geology 13, 721–733.

Peacock, D.C.P., Sanderson, D.J., 1996. Effects of propagation rate on displacement variations along faults. Journal of Structural Geology, 18, 311 – 320.

Pinto, L., Muñoz, C., Nalpas, T., Charrier, R., 2010. Role of sedimentation during basin inversion in analogue modelling. Journal of Structural Geology, 32, 554–565.

Pizzi, A., Galadini, F., 2009. Pre-existing cross-structures and active fault segmentation in the northern-central Apennines (Italy). Tectonophysics, 476, 304–319.

Pollard, D.D., Segall, P., 1987. Theoretical displacements and stresses near fractures in rock: with applications to faults, joints, veins, dikes, and solution surfaces. In, B.K. Atkinson (Ed.), Fracture Mechanics of Rock. Academic Press, London, p. 277-349.

Ramberg, H., 1981. Gravity, deformation and the Earth's crust. Academic Press, London.

Rovida, A., Camassi, R., Gasperini, P., and Stucchi, M. (eds.), 2011, CPTI11, the 2011 version of the Parametric Catalogue of Italian Earthquakes. Istituto Nazionale di Geofisica e Vulcanologia, Milano, Bologna, http://emidius.mi.ingv.it/CPTI, doi:10.6092/INGV.IT-CPTI11.

Sani, F., Del Ventisette, C., Montanari, D., Bendkik, A., Chenakeb, M., 2007. Structural evolution of the Rides Prerifaines (Morocco): structural and seismic interpretation and analogue modelling Experiments. International Journal of Earth Sciences, 96, 685–706.

Sassi, W., Colletta, B., Balé, P., Paquereau, T., 1993. Modelling of structural complexity in sedimentary basins: the role of pre-existing faults in thrust tectonics. Tectonophysics 226, 97–112.

Schlische, R.W., Young, S.S., Ackermann, R.V., Gupta, A., 1996. Geometry and scaling relations of a population of very small rift-related normal faults. Geology 24, 683– 686

Scholz, C.H., Cowie, P.A., 1990. Determination of geologic strain from fault slip data. Nature 346, 837– 839.

Scholz, C.H., 2002. The Mechanics of Earthquakes and Faulting. 2nd ed., 471 pp., Cambridge University Press, New York.

Schlagenhauf, A., Manighetti, I., Malavieille, J., Dominguez, S., 2008. Incremental growth of normal faults: Insights from a laser-equipped analog experiment. Earth and Planetary Science Letters 273 (2008) 299–311.

Selverstone, J., 1988. Evidence for east–west crustal extension in the Eastern Alps: implications for the unroofing history of the Tauern Window. Tectonics, 7, 87–105.

Tavarnelli, E., Decandia, F.A., Renda, P., Tramutoli, M., Gueguen, E., Alberti, M., 2001. Repeated reactivation in the Apennine-Maghrebide system, Italy: a possible example of fault-zone weakening? Geological

Society of London Special Publication 186, "The Nature and Tectonic Significance of Fault Zone Weakening". Holdsworth, R.E., Strachan, R.A., Maglouglin, J.F., Knipe, R.J., Eds., 273-286.

Tavarnelli, E., Prosser, G., 2003. The complete Apennines orogenic cycle preserved in a transient single outcrop near San Fele, Lucania, Southern Italy. Journal of the Geological Society of London, 160, 429-434.

Tavarnelli, E., Renda, P., Pasqui, V., Tramutoli, M., 2003. The effects of post-orogenic extension on different scales: an example from the Apennine-Maghrebide fold-and-thrust belt, SW Sicily. Terra Nova, 15, 1-7

Teng, L.S., 1996. Extensional collapse of the northern Taiwan mountain belt. Geology, 24, 10, 949-952.

Thielicke, W., 2014. The Flapping Flight of Birds - Analysis and Application. Phd thesis, Rijksuniversiteit Groningen.

Thielicke, W., Stamhuis, E.J., 2014. PIVlab – Towards User-friendly, Affordable and Accurate Digital Particle Image Velocimetry in MATLAB. Journal of Open Research Software 2(1):e30, doi:http://dx.doi.org/10.5334/jors.bl.

Torabi, A., Berg, S.S. 2011. Scaling of fault attributes: A review. Marine and Petroleum Geology, 28 (8), 1444-1460. doi:10.1016/j.marpetgeo.2011.04.00.

Toscani, G., Bonini, L., Ahmad, M.I., Di Bucci, D., Di Giulio, A., Seno, S., Galuppo, C., 2014. Opposite verging chains sharing the same foreland: kinematics and interaction through analogue models (Central Po Plain, Italy). Tectonophysics, 633, 268-282. doi:10.1016/j.tecto.2014.07.019.

Villemin, T., Angelier, J., Sunwoo, C., 1995. Fractal distribution of fault length and offsets: implications of brittle deformation evaluation—Lorraine Coal Basin. In: Barton, C.C., La Pointe, P.R. (Eds.), Fractal in the Earth Sciences. Plenum, New York, pp. 205– 226.

Valensise, G., Pantosti D., 2001. The investigation of potential earthquake sources in peninsular Italy: a review. J. Seismol., 5, 287-306, doi: 10.1023/A:1011463223440.

Viola, G., Odonne, F., Mancktelow, N.S., 2004. Analogue modelling of reverse fault reactivation in strike-slip and transpressive regimes: Application to the Giudicarie fault system, Italian Eastern Alps. Journal of Structural Geology, 26 (3), 401-418, doi: 10.1016/j.jsg.2003.08.014

Walsh, J.J., Nicol, A., Childs, C., 2002. An alternative model for the growth of faults. Journal of Structural Geology 24, 1669– 1675.

Walsh, J.J., Watterson, J., 1987. Distributions of cumulative displacement and seismic slip on a single normal fault surface. Journal of Structural Geology 9, 1039– 1046.

Wells, D.L., Coppersmith, K.J., 1994. New empirical relationships among magnitude, rupture length, rupture width, rupture area, and surface displacement. Bulletin of the Seismological Society of America, 84, 974–1002.

Wernicke, B., 1981. Low-angle normal faults in the Basin and range province: nappe tectonics in an extending orogen. Nature, 291, 645-648.

Wesnousky, S.G., 2008. Displacement and geometrical characteristics of earthquake surface ruptures: Issues and implications for seismic hazard analysis and the earthquake rupture process. Bulletin of the Seismological Society of America, 98, 1609-1632, 2008.

Whipp, P.S., Jackson, C.A.L., Gawthorpe, R.L., Dreyer, T., Quinn, D., 2014. Fault array evolution above a reactivated rift fabric; a subsurface example from the northern Horda Platform fault array, Norwegian North Sea. Basin Res., 26, 523–549.

Wilkins, S.J., Gross, M.R., 2002. Normal fault growth in layered rocks at Split Mountain, Utah: influence of mechanical stratigraphy on dip linkage, fault restriction and fault scaling. Journal of Structural Geology 24, 1413– 1429.

Withjack, M.O., Schlische, R.W., 2006. Geometric and experimental models of extensional fault-bend folds. Geological Society Special Publication, 253, 285-305.

Withjack, M.O., Schlische, R.W., Henza, A.A., 2007. Scaled experimental models of extension: dry sand vs. wet clay. Houston Geological Survey Bulletin, 49, 31-49.

TABLES

Table 1. Ranking chart of the relative influence (in percent) of precut onto several observables with respect to the isotropic experiment. Legend: negligible influence or no influence at all for P ≤ 25% (regular); moderate influence for 25% < P ≤ 50% (*italics*); high influence for P > 50% (**bold**). Notice that E3 is unimodal in both stages and E5 is unimodal only in the Middle Stage. All other profiles are basically bimodal in both stages.

Middle Stage

Observable	Synthetic attitude			Antithetic attitude		
	E2 (30°)	E3 (45°)	E4 (60°)	E5 (30°)	E6 (45°)	E7 (60°)
Total displacement	**67%**	1%	*42%*	16%	**77%**	2%
Apparent segmentation	**100%**	13%	**100%**	**54%**	**100%**	*34%*
Dmax value	15%	22%	7%	*32%*	**56%**	1%
Dmax position	**63%**	22%	5%	**63%**	14%	6%
Length	*42%*	*26%*	*37%*	20%	*37%*	15%
All observables (mean)	**57%**	17%	*38%*	*37%*	**57%**	11%

Late Stage

Observable	Synthetic attitude			Antithetic attitude		
	E2 (30°)	E3 (45°)	E4 (60°)	E5 (30°)	E6 (45°)	E7 (60°)
Total displacement	**52%**	12%	*25%*	*28%*	**52%**	3%
Apparent segmentation	**100%**	3%	**100%**	*40%*	**53%**	**56%**
Dmax value	14%	12%	0%	1%	*29%*	9%
Dmax position	**61%**	21%	14%	5%	**61%**	19%
Length	17%	22%	0%	17%	*33%*	0%
All observables (mean)	*49%*	14%	*28%*	18%	*46%*	18%

	Both Stages					
All observables (mean)	**53%**	15%	*33%*	*28%*	**51%**	15%

FIGURE CAPTIONS

Figure 1. Plan view (a) and cross-sectional view (b) of the experimental apparatus. Orange color marks the mobile parts.

Figure 2. Map views of analyses carried out in one of the isotropic experiments (E1A) as it progresses through the Early, Middle, and Late stages of master fault activity. First row (a, f, k): slope of the free surface highlighting the main fault traces. Second row (b, g, l): mapped new faults and free-surface topography. Third row (c, h, m): incremental horizontal displacement field calculated using the D.I.C. (Displacement Image Correlation) method. Fourth row (d, i, n): strike-parallel component of the horizontal displacement field. Fifth row (e, j, o): strain distribution. The thin dashed line labelled with M.F. (Master Fault) marks the border of the buried master fault in each panel. The thick dashed line marks the region of interest (i.e. the area outside which unwanted effects of the model edges may occur) in each panel.

Figure 3. Profiles of the cumulative displacement of E1A (a) and point data of all isotropic experiments in the Middle (b) and Late (c) stages. Gray bars on the horizontal axes mark the position of the master fault. Gray lateral areas mark the areas outside the Region Of Interest (ROI).

Figure 4. Setup of the six experiments with precut (map view). Orange color marks the mobile parts of the apparatus. See Fig. 1 for the cross-sectional view.

Figure 5. Map view of the experiments with synthetic precuts at the three stages of evolution showing faults and color-coded topography. Thick black hachured lines represent new faults or parts of the precut displaying significant offset during the relevant stage. Thin lines represent primary (solid) and minor (dashed) fractures. Other symbols as in Fig. 2.

Figure 6. Map view of the three development stages of the experiments with synthetic precut showing the incremental horizontal displacement field. Small arrows are horizontal displacement vectors. Displacement

magnitude is shown in colors. Faults, fractures, and precut symbols are as in Figure 5. Other symbols as in Fig. 2.

Figure 7. Profiles of cumulative displacement along the precut (a, c, e) and along newly-formed surface faults (b, d, f) in experiments with synthetic precuts. Gray bars on the horizontal axes mark the position of the master fault. Gray lateral areas mark the areas outside the Region Of Interest (ROI). Gray bars along section #12 show the position of the precut.

Figure 8. Map view of the experiments with antithetic precuts at the three stages of evolution showing faults and color-coded topography. Thick black hachured lines represent new faults or parts of the precut displaying significant offset during the relevant stage. Thin lines represent primary (solid) and minor (dashed) fractures. Other symbols as in Fig. 2.

Figure 9. Map view of the three development stages of experiments with antithetic precut showing the incremental horizontal displacement field. Small arrows are horizontal displacement vectors. Displacement magnitude is shown in colors. Faults, fractures, and precut symbols are as in Figure 5. Other symbols as in Fig. 2.

Figure 10. Profiles of cumulative displacement along the precut (a, c, e) and along newly-formed surface faults (b, d, f) in experiments with antithetic precuts. Gray bars on the horizontal axes mark the position of the master fault. Gray lateral areas mark the areas outside the Region Of Interest (ROI). Gray bars along section #12 show the position of the precut.

Figure 11. a) Diagrams showing displacement point data collected along the fault surface trace for the set of three isotropic experiments and their Gaussian fit along with 95% confidence and prediction intervals; b) Comparison between linear, circular, and Gaussian models of displacement (both axes are normalized); c) RMS of deviations between displacement point data and the linear, circular, and Gaussian models.

Figure 12. a) Displacement profiles of experiments with precut; b) comparison between the Gaussian fit of the isotropic experiment set (same as Fig. 11a) and point data collected along the fault surface trace of experiments with precut; c) RMS of deviations between experimental point data and the Gaussian model; d) Dmax value of the Gaussian model of isotropic experiments (along with 95% prediction interval) compared with Dmax values of experiments with precut; e) Dmax point position of the Gaussian model of isotropic experiments compared with Dmax point position of experiments with precut. Gray bars on the horizontal axes mark the position of the master fault. f) Surface fault length measured in all experiments.

Figure 13. Diagram showing maximum displacement (Dmax) vs fault length (L) of the experiments carried out in this work and those derived from field data (Muraoka and Kamata, 1983; Krantz, 1988; Opheim and Gudmundsson, 1989; Scholz and Cowie, 1990; Peacock and Sanderson, 1991; Dawers et al., 1993; Wilkins and Gross, 2002), from quarries (Schlische et al., 1996), from mines (Walsh and Watterson, 1987; Scholz and Cowie, 1990; Villemin et al., 1995), and from subsurface data (Walsh et al., 2002). The fitting line for normal faults is from Kim and Sanderson (2005).

Figure 14. a) Tectonic sketch map of the northern North Sea. b) Map showing the non-colinear fault sets in the northern Horda Platform (from Duffy et al., 2015). Thick black lines are faults formed in the first rift phase; gray lines are faults from the second rift phase. Labels refer to faults discussed in the text. The inset synthetizes the trend of extensional faults in the area. c) Map view of the Central Apennines. The inset synthetizes the major structural trends of the three, successive tectonic phases (from Pizzi and Galadini, 2009). d) Tectonic sketch map of the Central Apennines (modified from Vezzani et al., 2009). Dark gray areas mark the main Plio-Quaternary basins. e) Evolutionary sketch of the Fucino Basin (modified from Cavinato et al., 2002); gray areas represents the location of lacustrine deposits.

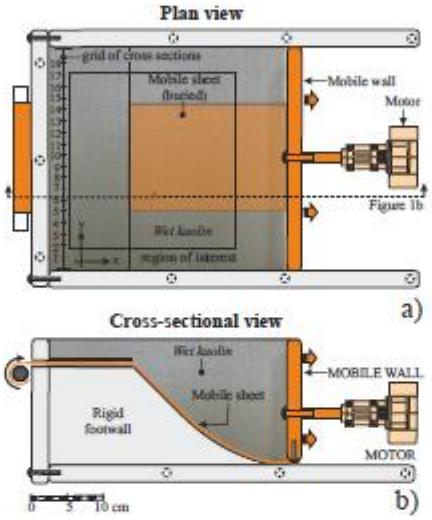

Figure 1. Plan view (a) and cross-sectional view (b) of the experimental apparatus. Orange color marks the mobile parts.

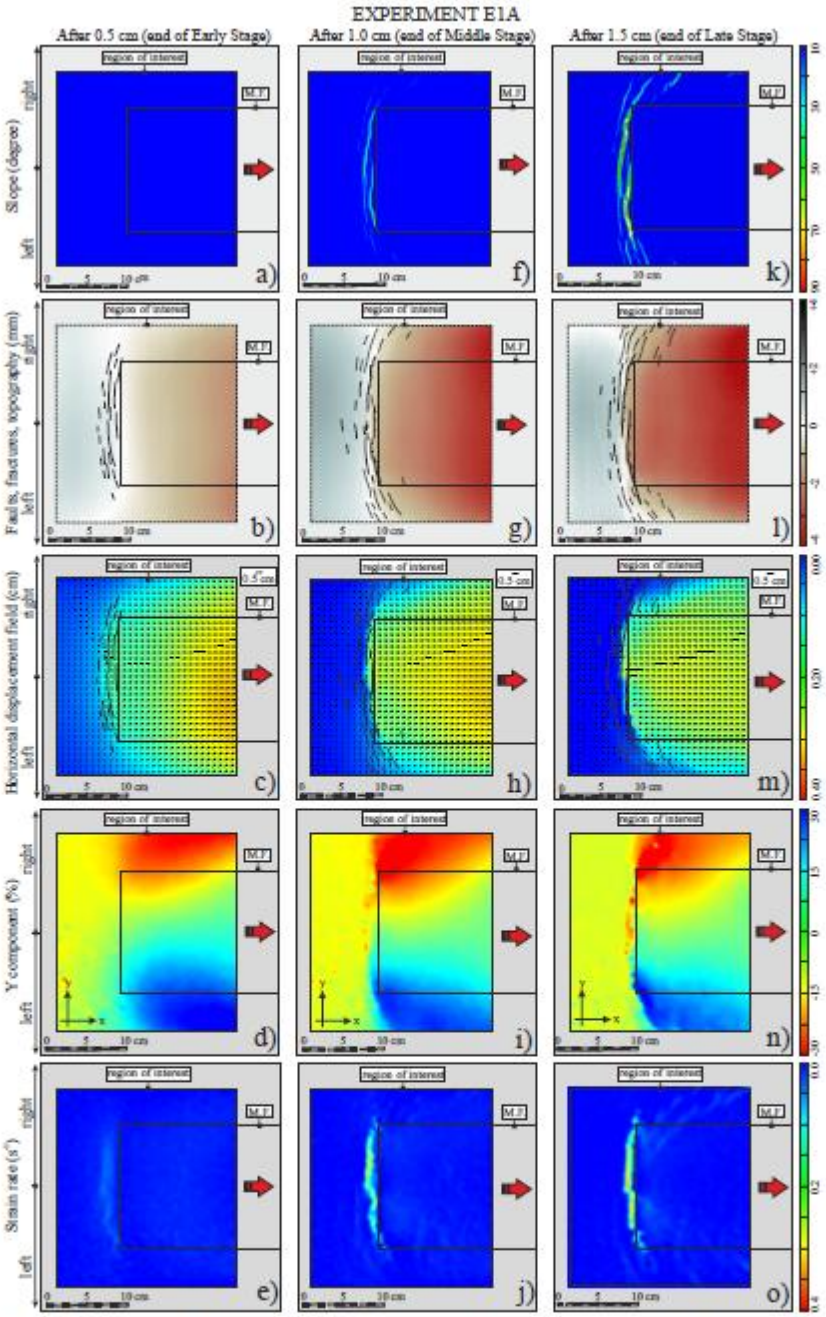

Figure 2. Map views of analyses carried out in one of the isotropic experiments (E1A) as it progresses through the Early, Middle, and Late stages of master fault activity. First row (a, f, k): slope of the free surface highlighting the main fault traces. Second row (b, g, l): mapped new faults and free-surface topography. Third row (c, h, m): incremental horizontal displacement field calculated using the D.I.C. (Displacement Image Correlation) method. Fourth row (d, i, n): strike-parallel component of the horizontal displacement field. Fifth row (e, j, o): strain distribution. The thin dashed line labelled with M.F. (Master Fault) marks the border of the buried master fault in each panel. The thick dashed line marks the region of interest (i.e. the area outside which unwanted effects of the model edges may occur) in each panel.

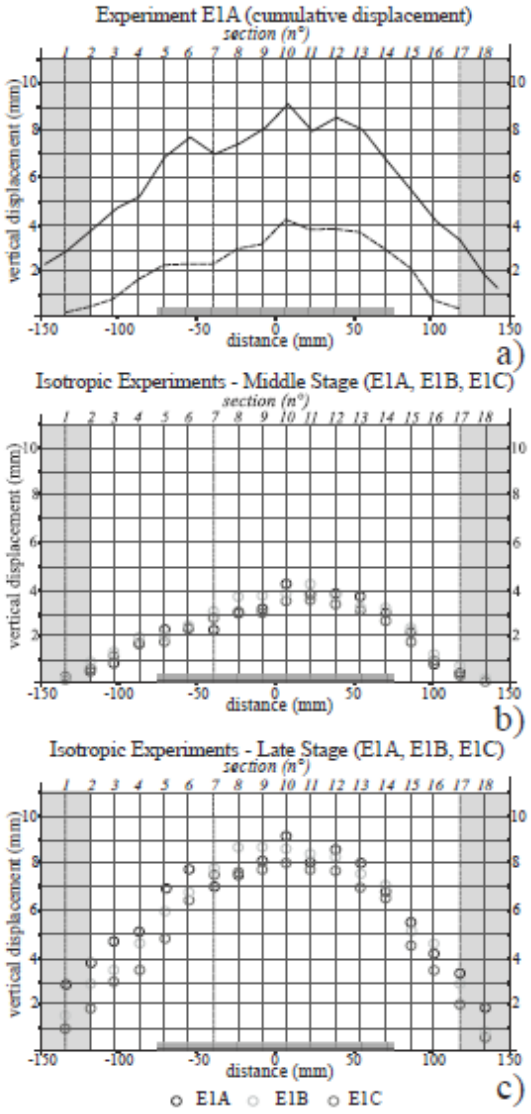

Figure 3. Profiles of the cumulative displacement of E1A (a) and point data of all isotropic experiments in the Middle (b) and Late (c) stages. Gray bars on the horizontal axes mark the position of the master fault. Gray lateral areas mark the areas outside the Region Of Interest (ROI).

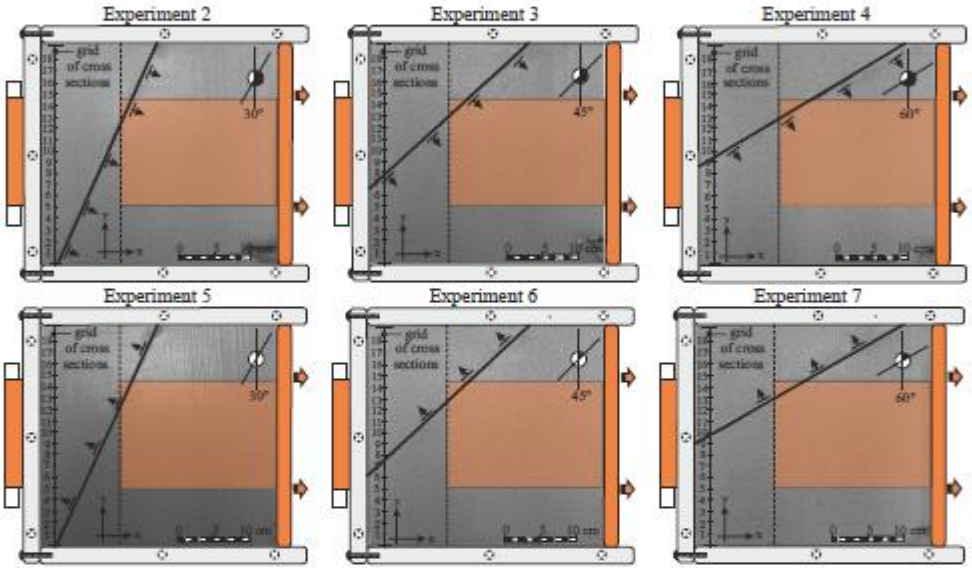

Figure 4. Setup of the six experiments with precut (map view). Orange color marks the mobile parts of the apparatus. See Fig. 1 for the cross-sectional view.

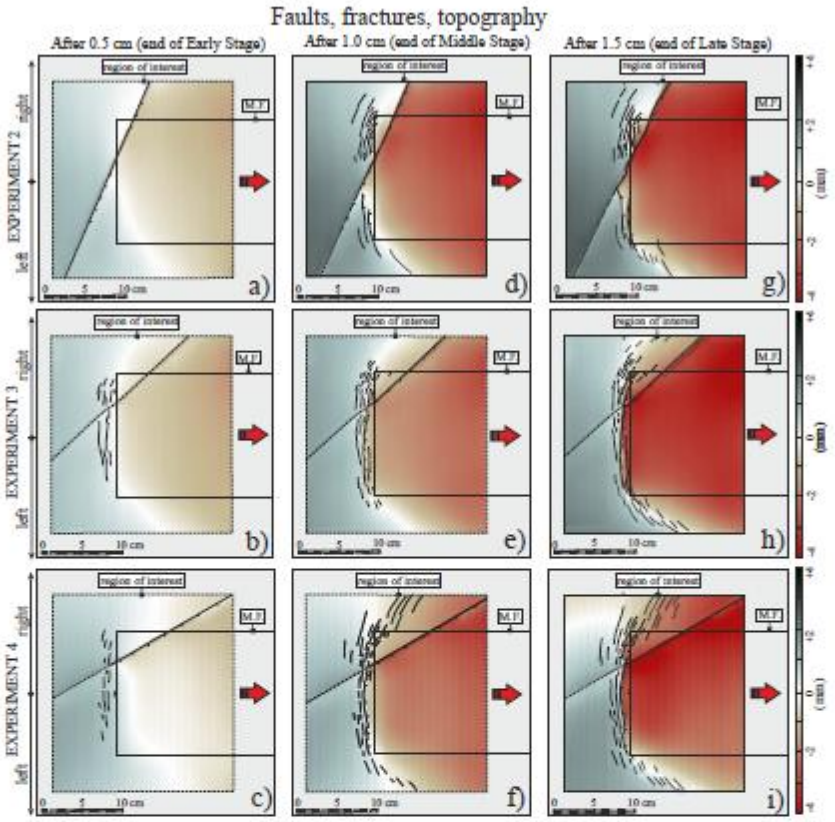

Figure 5. Map view of the experiments with synthetic precuts at the three stages of evolution showing faults and color-coded topography. Thick black hachured lines represent new faults or parts of the precut displaying significant offset during the relevant stage. Thin lines represent primary (solid) and minor (dashed) fractures. Other symbols as in Fig. 2.

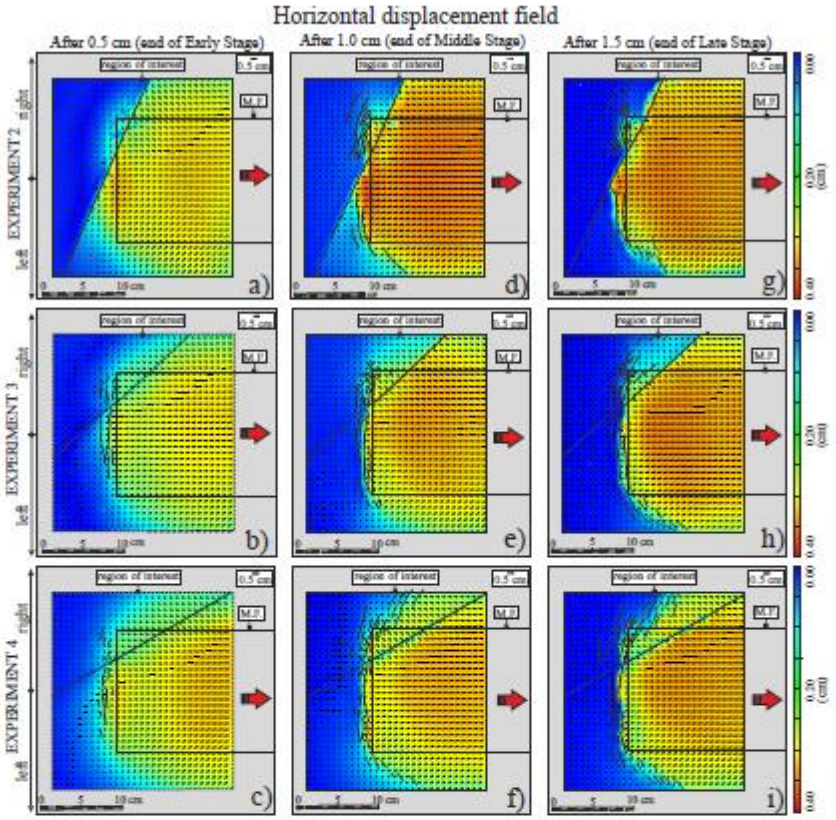

Figure 6. Map view of the three development stages of the experiments with synthetic precut showing the incremental horizontal displacement field. Small arrows are horizontal displacement vectors. Displacement magnitude is shown in colors. Faults, fractures, and precut symbols are as in Figure 5. Other symbols as in Fig. 2.

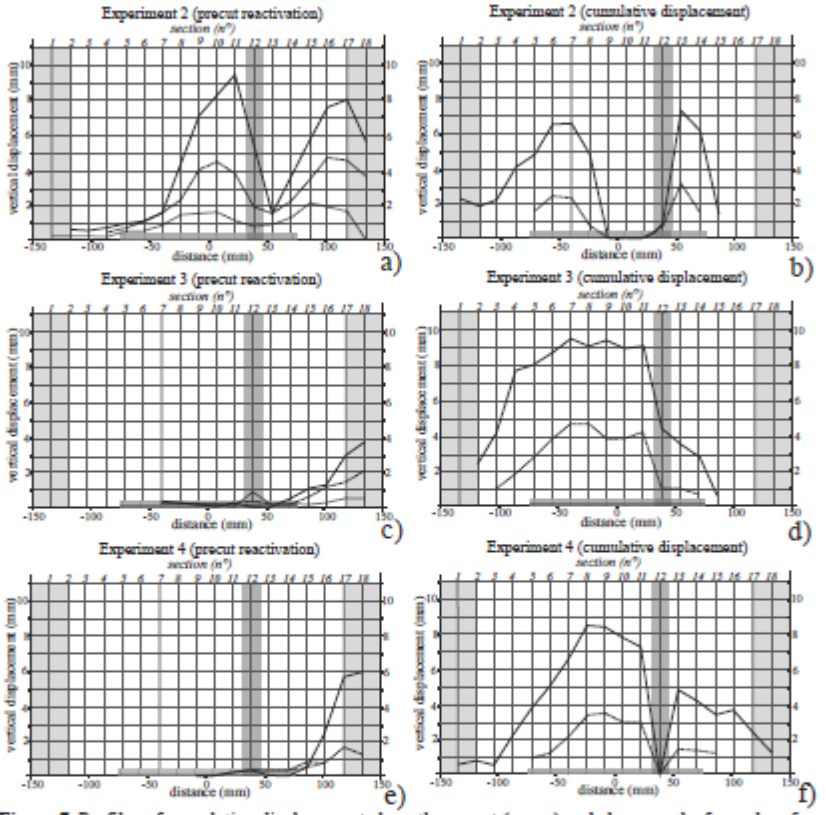

Figure 7. Profiles of cumulative displacement along the precut (a, c, e) and along newly-formed surface faults (b, d, f) in experiments with synthetic precuts. Gray bars on the horizontal axes mark the position of the master fault. Gray lateral areas mark the areas outside the Region Of Interest (ROI). Gray bars along section #12 show the position of the precut.

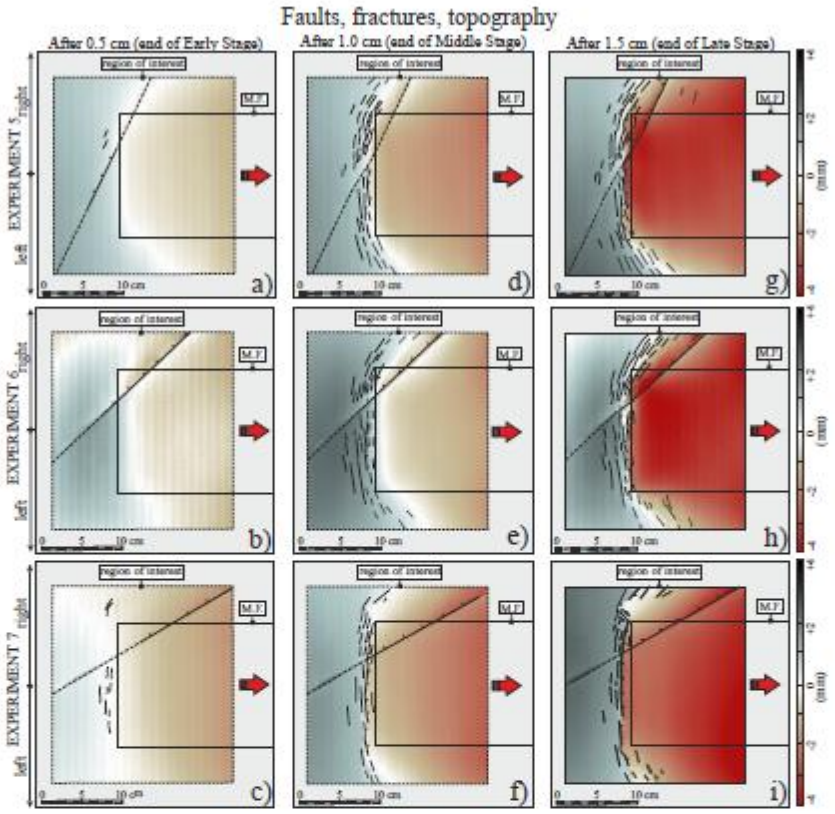

Figure 8. Map view of the experiments with antithetic precuts at the three stages of evolution showing faults and color-coded topography. Thick black hachured lines represent new faults or parts of the precut displaying significant offset during the relevant stage. Thin lines represent primary (solid) and minor (dashed) fractures. Other symbols as in Fig. 2.

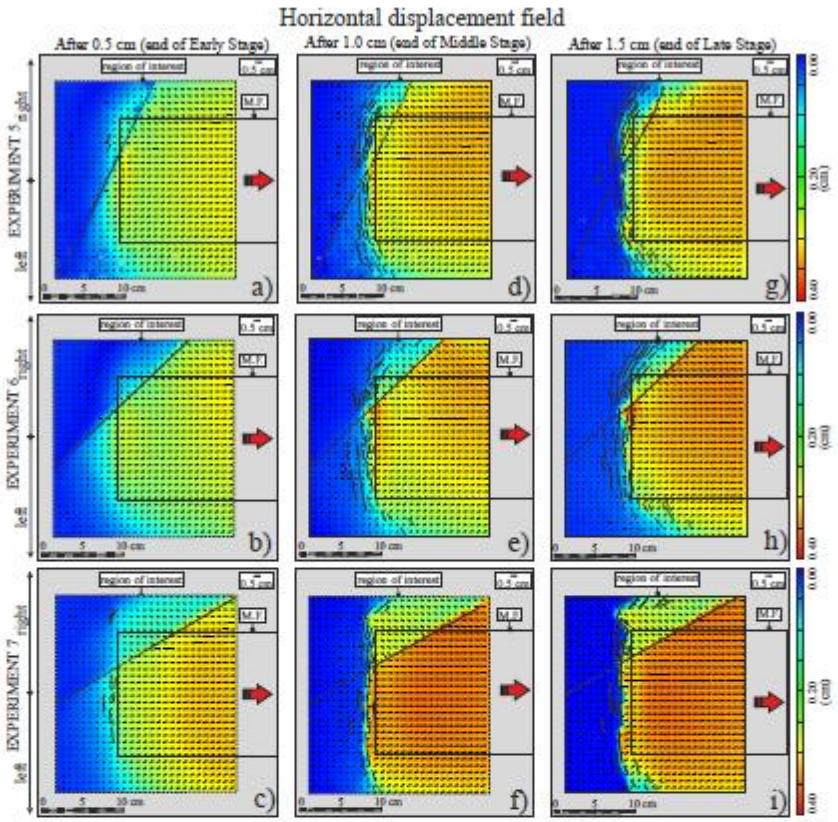

Figure 9. Map view of the three development stages of experiments with antithetic precut showing the incremental horizontal displacement field. Small arrows are horizontal displacement vectors. Displacement magnitude is shown in colors. Faults, fractures, and precut symbols are as in Figure 5. Other symbols as in Fig. 2.

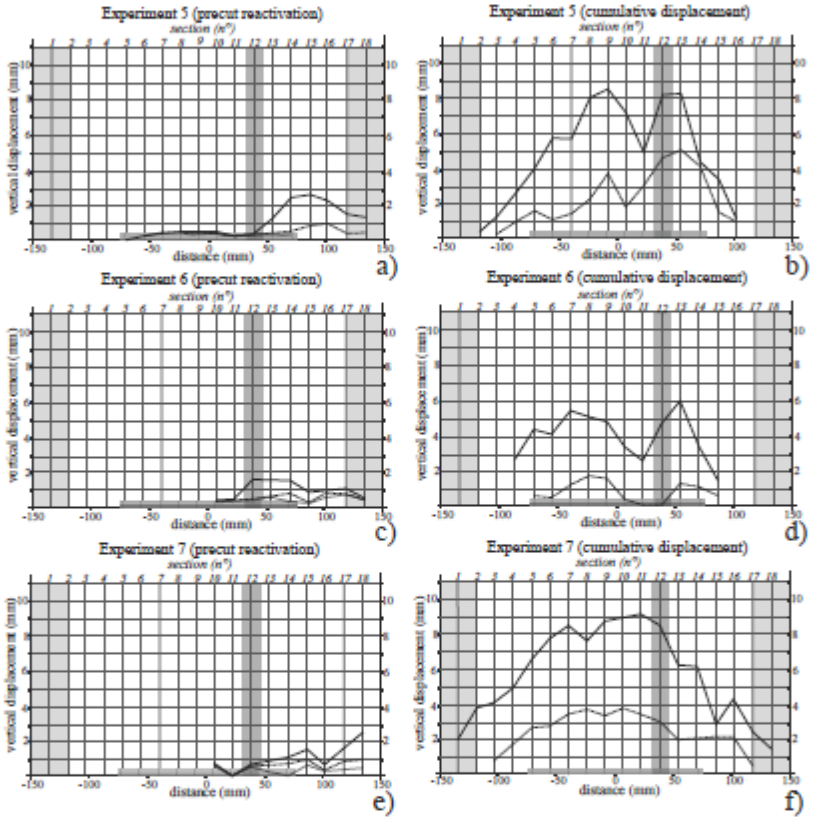

Figure 10. Profiles of cumulative displacement along the precut (a, c, e) and along newly-formed surface faults (b, d, f) in experiments with antithetic precuts. Gray bars on the horizontal axes mark the position of the master fault. Gray lateral areas mark the areas outside the Region Of Interest (ROI). Gray bars along section #12 show the position of the precut.

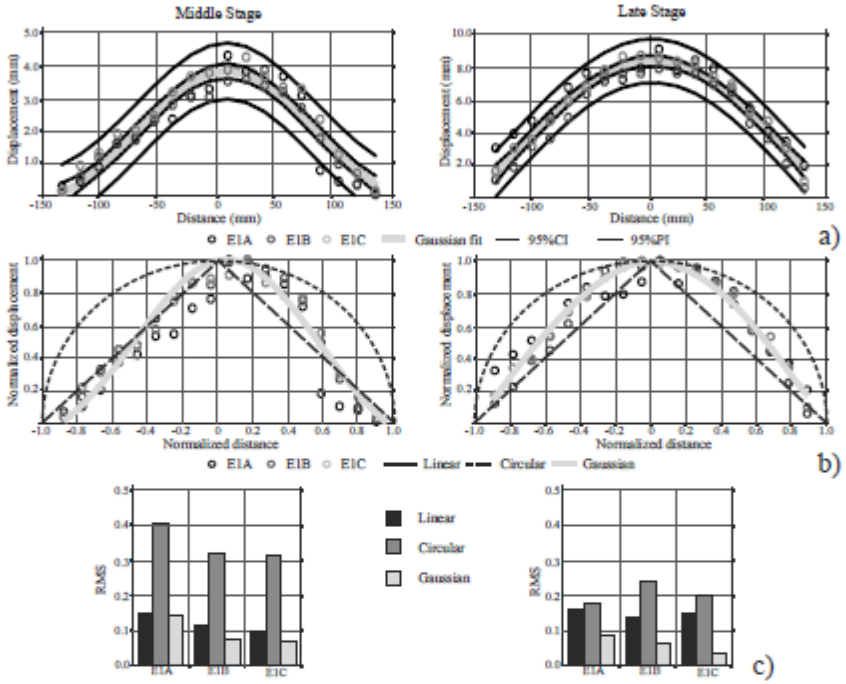

Figure 11. a) Diagrams showing displacement point data collected along the fault surface trace for the set of three isotropic experiments and their Gaussian fit along with 95% confidence and prediction intervals; b) Comparison between linear, circular, and Gaussian models of displacement (both axes are normalized); c) RMS of deviations between displacement point data and the linear, circular, and Gaussian models.

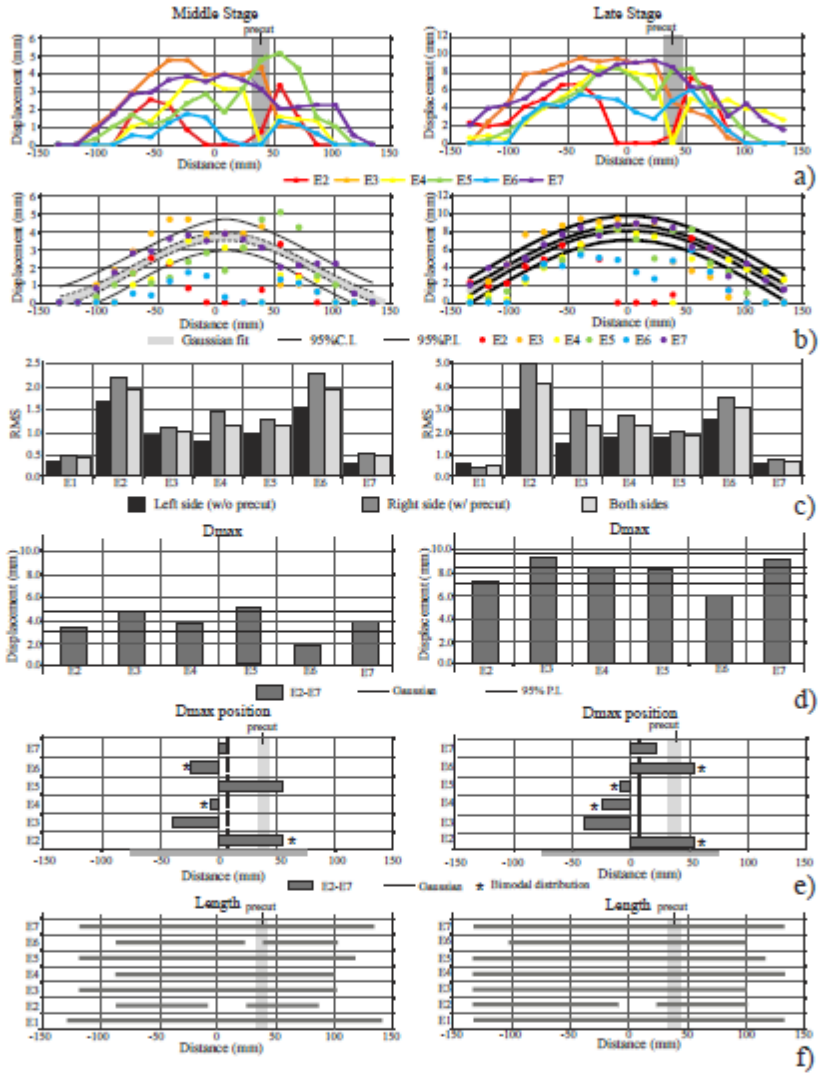

Figure 12. a) Displacement profiles of experiments with precut; b) comparison between the Gaussian fit of the isotropic experiment set (same as Fig. 11a) and point data collected along the fault surface trace of experiments with precut; c) RMS of deviations between experimental point data and the Gaussian model; d) Dmax value of the Gaussian model of isotropic experiments (along with 95% prediction interval) compared with Dmax values of experiments with precut; e) Dmax point position of the Gaussian model of isotropic experiments compared with Dmax point position of experiments with precut. Gray bars on the horizontal axes mark the position of the master fault. f) Surface fault length measured in all experiments.

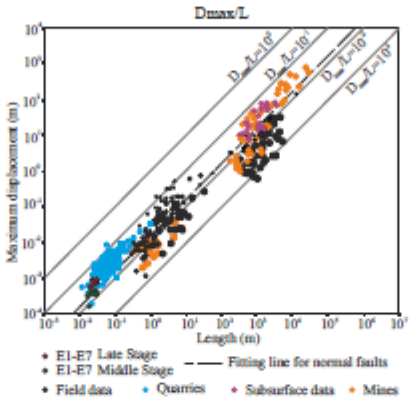

Figure 13. Diagram showing maximum displacement (Dmax) vs fault length (L) of the experiments carried out in this work and those derived from field data (Muraoka and Kamata, 1983; Krantz, 1988; Opheim and Gudmundsson, 1989; Scholz and Cowie, 1990; Peacock and Sanderson, 1991; Dawers et al., 1993; Wilkins and Gross, 2002), from quarries (Schlische et al., 1996), from mines (Walsh and Watterson, 1987; Scholz and Cowie, 1990; Villemin et al., 1995), and from subsurface data (Walsh et al., 2002). The fitting line for normal faults is from Kim and Sanderson (2005).

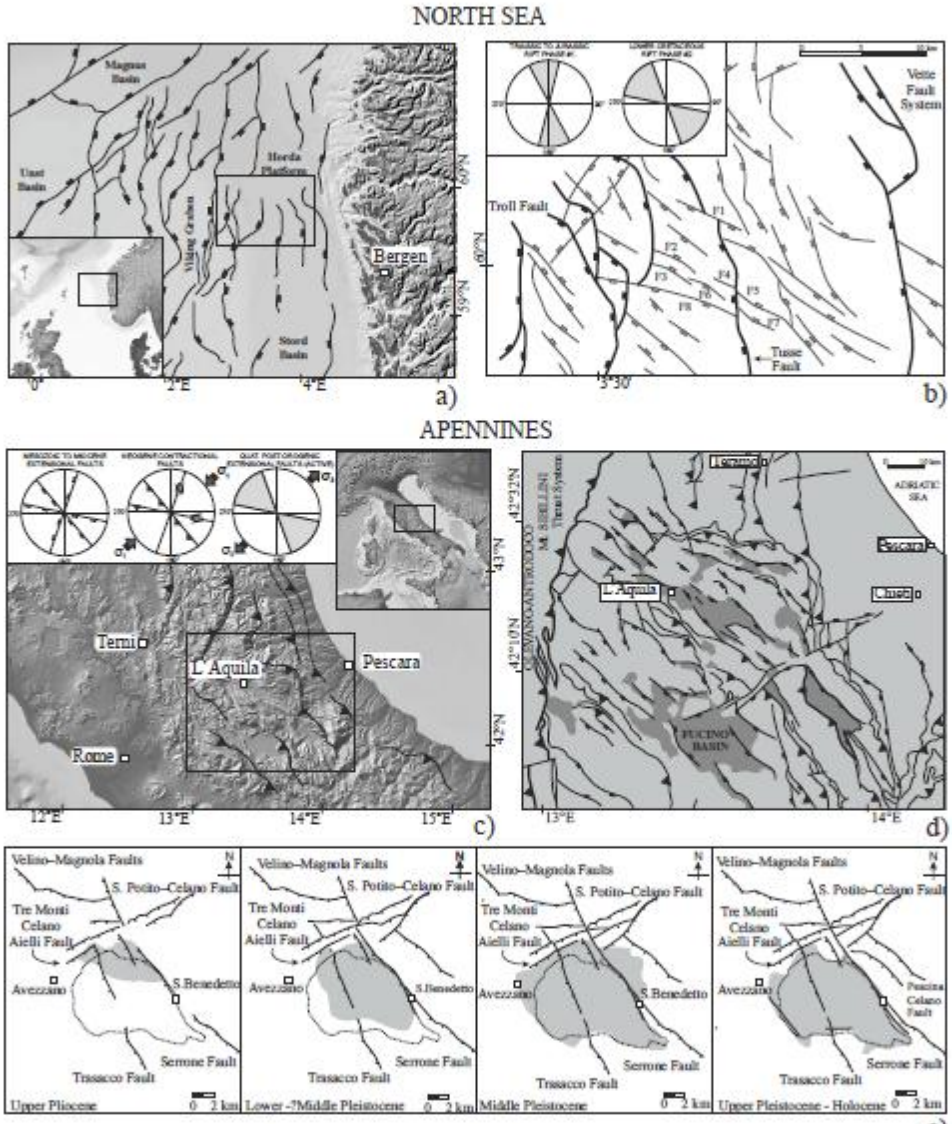

Figure 14. a) Tectonic sketch map of the northern North Sea. b) Map showing the non-colinear fault sets in the northern Horda Platform (from Duffy et al., 2015). Thick black lines are faults formed in the first rift phase; gray lines are faults from the second rift phase. Labels refer to faults discussed in the text. The inset synthetizes the trend of extensional faults in the area. c) Map view of the Central Apennines. The inset synthetizes the major structural trends of the three, successive tectonic phases (from Pizzi and Galadini, 2009). d) Tectonic sketch map of the Central Apennines (modified from Vezzani et al., 2009). Dark gray areas mark the main Plio-Quaternary basins. e) Evolutionary sketch of the Fucino Basin (modified from Cavinato et al., 2002); gray areas represents the location of lacustrine deposits.

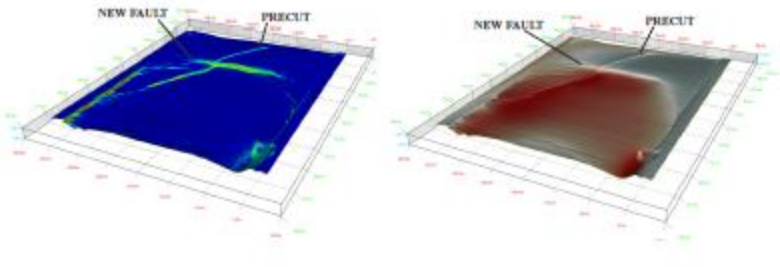

Graphical abstract

Highlights

- We use wet-clay analog models to simulate isolated initially-blind normal faults.
- We analyze the interaction of surface normal faults with inherited discontinuities.
- Inherited discontinuities strongly affect fault development at the Earth's surface.
- The influence of a discontinuity strongly depends on its orientation relative to the fault.
- We provide a ranking chart to assess fault-to-discontinuity interactions.